A biomimetic vision-based hovercraft accounts for bees' complex behaviour in various corridors

Frédéric L. Roubieu, Julien R. Serres, Fabien Colonnier, Nicolas Franceschini, Stéphane Viollet, Franck Ruffier

OPEN ACCESS
IOP Publishing
Bioinspiration & Biomimetics
Bioinspir. Biomim. **9** (2014) 036003 (22pp)
doi:10.1088/1748-3182/9/3/036003

A biomimetic vision-based hovercraft accounts for bees' complex behaviour in various corridors*

Frédéric L Roubieu, Julien R Serres, Fabien Colonnier, Nicolas Franceschini, Stéphane Viollet and Franck Ruffier[1]

Aix-Marseille Université, CNRS, ISM UMR 7287, 13288, Marseille cedex 09, France

E-mail: frederic.roubieu@univ-amu.fr, julien.serres@univ-amu.fr, fabien.colonnier@univ-amu.fr, nicolas.franceschini@univ-amu.fr, stephane.viollet@univ-amu.fr and franck.ruffier@univ-amu.fr

Received 2 May 2013, revised 14 October 2013
Accepted for publication 17 December 2013
Published 11 March 2014

Abstract

Here we present the first systematic comparison between the visual guidance behaviour of a biomimetic robot and those of honeybees flying in similar environments. We built a miniature hovercraft which can travel safely along corridors with various configurations. For the first time, we implemented on a real physical robot the 'lateral optic flow regulation autopilot', which we previously studied computer simulations. This autopilot inspired by the results of experiments on various species of hymenoptera consists of two intertwined feedback loops, the speed and lateral control loops, each of which has its own optic flow (OF) set-point. A heading-lock system makes the robot move straight ahead as fast as 69 cm s^{-1} with a clearance from one wall as small as 31 cm, giving an unusually high translational OF value (125° s^{-1}). Our biomimetic robot was found to navigate safely along straight, tapered and bent corridors, and to react appropriately to perturbations such as the lack of texture on one wall, the presence of a tapering or non-stationary section of the corridor and even a sloping terrain equivalent to a wind disturbance. The front end of the visual system consists of only two local motion sensors (LMS), one on each side. This minimalistic visual system measuring the lateral OF suffices to control both the robot's forward speed and its clearance from the walls without ever measuring any speeds or distances. We added two additional LMSs oriented at +/−45° to improve the robot's performances in stiffly tapered corridors. The simple control system accounts for worker bees' ability to navigate safely in six challenging environments: straight corridors, single walls, tapered corridors, straight corridors with part of one wall moving or missing, as well as in the presence of wind.

Keywords: optic flow (OF), autonomous guidance, collision avoidance, urban canyon navigation, hovercraft, biorobotics, bionics

(Some figures may appear in colour only in the online journal)

1. Introduction

The bio-inspired robots constructed over the past 25 years have largely contributed to create the field of Biorobotics, in which natural principles or systems are abstracted from an animal and implemented onboard a real robot. Beyond their possible usefulness in the field of Robotics, these biomimetic robots can be used as models to test biological hypotheses using the

* The following video shows the LORA robot visually guiding itself in various tunnels: www.dailymotion.com/embed/video/xuggrs

[1] Author to whom any correspondence should be addressed.

rigorous experiments imposed by the real world (Franceschini *et al* 1992, Webb 2001, Ijspeert *et al* 2007). Biorobotics therefore provides us with a transdisciplinary approach, which can help us to identify and investigate worthwhile issues in the field of biological sensory-motor control systems. Over the past 25 years, several optic flow (OF)-based strategies have been implemented on various robots. The present study is the first, however, to account systematically for a series of flying abilities observed in bees by several authors in an exhaustive set of corridors, whereas the other bio-inspired strategies do not account for all the bees' behaviours in this same set of corridor.

Flying bees are able to perform some exquisitely difficult tasks when flying through unknown, unpredictable environments without using any emissive sensors to assess their speed or the distance to obstacles, relying mainly on the OF cues generated by their own motion (Horridge 1987). Honeybees also possess velocity-tuned (VT) neurons responding monotonically to the optic flow (Ibbotson 2001).

The OF is the angular speed ω (magnitude in $^\circ$ s^{-1}) at which any contrasting object moves past the subjects eye (Whiteside and Samuel 1970, Koenderink and van Doorn 1987). Flying bees use lateral translational OF:

- to avoid lateral obstacles (Kirchner and Srinivasan 1989, Srinivasan *et al* 1991, Serres *et al* 2008b, Dyhr and Higgins 2010, Baird and Dacke 2012),
- to control their speed depending on the local corridor width (Srinivasan *et al* 1996, Baird *et al* 2006, 2010, Portelli *et al* 2010, 2011, Baird and Dacke 2012),
- to control their speed against wind (Barron and Srinivasan 2006) and
- to control their speed or their position in the presence of moving walls (Kirchner and Srinivasan 1989, Srinivasan *et al* 1991, Baird *et al* 2005).

Kirchner and Srinivasan (1989) observed that honeybees flying along a narrow corridor tended to maintain equidistance from the stationary lateral walls. These authors therefore suggested that this centring response might involve balancing the apparent motion of the images of the walls perceived by their two compound eyes (Kirchner and Srinivasan 1989, Srinivasan *et al* 1991).

Recent behavioural experiments have shown that *honeybees do not in fact systematically keep to the midline of corridors* (Serres *et al* 2008b) and may instead adopt *wall-following* behaviour by navigating off-centred along a corridor. The latter behaviour actually makes sense, as insects must also be able to cope with a single-sided contrasting environment.

In other studies, honeybees flying along a narrow tapered corridor have been found to keep proportional their flight speed and the local corridor width: the authors suggested that bees might proceed by regulating the total OF experienced on either sides (Srinivasan *et al* 1996).

Other observations and experiments have shown that flying insects use their ventral translational OF to control their altitude (Ruffier and Franceschini 2005, Baird *et al* 2006, Franceschini *et al* 2007, Portelli *et al* 2010) as well as responding to the expanding OF (Wagner 1982, Tammero and Dickinson 2002, Straw *et al* 2010, Baird *et al* 2013).

Several OF-based strategies were implemented in physical robots to obtain centring behaviour while concomitantly controlling the forward speed:

- using the OF balance strategy along with OF-based speed control (mobile robots: Santos-Victor *et al* (1995), Weber *et al* (1997), Baratoff *et al* (2000), Argyros *et al* (2004))
- or the 'bio-inspired visuomotor convergence' theory (aerial robot: Conroy *et al* (2009); mobile robot: Humbert and Hyslop (2010); hovercraft: Fuller and Murray (2011)).

Each of these OF-based control strategies gives different behaviours and none of them accounts for insect's wall-following behaviour.

In previous computer simulations, the autopilot based on the *dual OF regulator* called lateral optic flow regulation autopilot (LORA) automatically controls both the speed and the clearance from the walls (Serres *et al* 2008a). Preliminary results presented in Roubieu *et al* (2012) showed that a robotic hovercraft can perform not only *centring* but also *wall-following* tasks.

In this paper, the LORA autopilot based on the *dual OF regulator* was implemented and tested onboard a small robotic hovercraft (figure 1*(A)*) placed in a similar corridor to those used to study honeybees' behaviour. Other authors have endowed robots with OF-based visual guidance systems with small magnitude of measured OFs (less than 60–70° s^{-1}) in the case of aerial robots (Zufferey and Floreano 2006, Zufferey *et al* 2007) and in that of mobile robots under steady-state conditions (Humbert and Hyslop 2010).

However, it has never been previously established that robotic visual guidance is possible at much higher OF values ($\geqslant$125° s^{-1}) in a real physical robot travelling at high speed (69 cm s^{-1}) near a wall (31 cm away), as achieved here with the LORA robot. Given the proximity of the obstacle, the model had to be validated by performing physical tests: an account of these tests is presented in this paper.

In this study, the LORA robot was equipped:

- with a heading-lock system ensuring that the robot will move quickly straight ahead and therefore receives a purely translational OF
- and with a visual system consisting of a minimalistic fly-inspired compound eye comprising two pairs of OF sensors oriented laterally—one of either side—with the addition of two pairs oriented at $\pm 45^\circ$ in section 5.

Our robotic platform is described in detail in section 2. The LORA autopilot based on a heading-lock system and the *dual OF regulator* mounted onboard the hovercraft to guide it in unknown environments are described in section 3. The experimental results obtained with the actual physical robot equipped with two pairs of pixels and the *dual OF regulator* serving to guide the robot along straight, tapered and bending corridors are presented in section 4. The implementation of frontal eyes to improve the lateral obstacle avoidance performances obtained in highly challenging corridors is discussed in section 5. In section 7, the LORA robot's trajectories are systematically compared with those of bees' trajectories in a complete set of similar corridors in the presence of similar disturbances: the results of these systematic comparisons are summarized in the final figure.

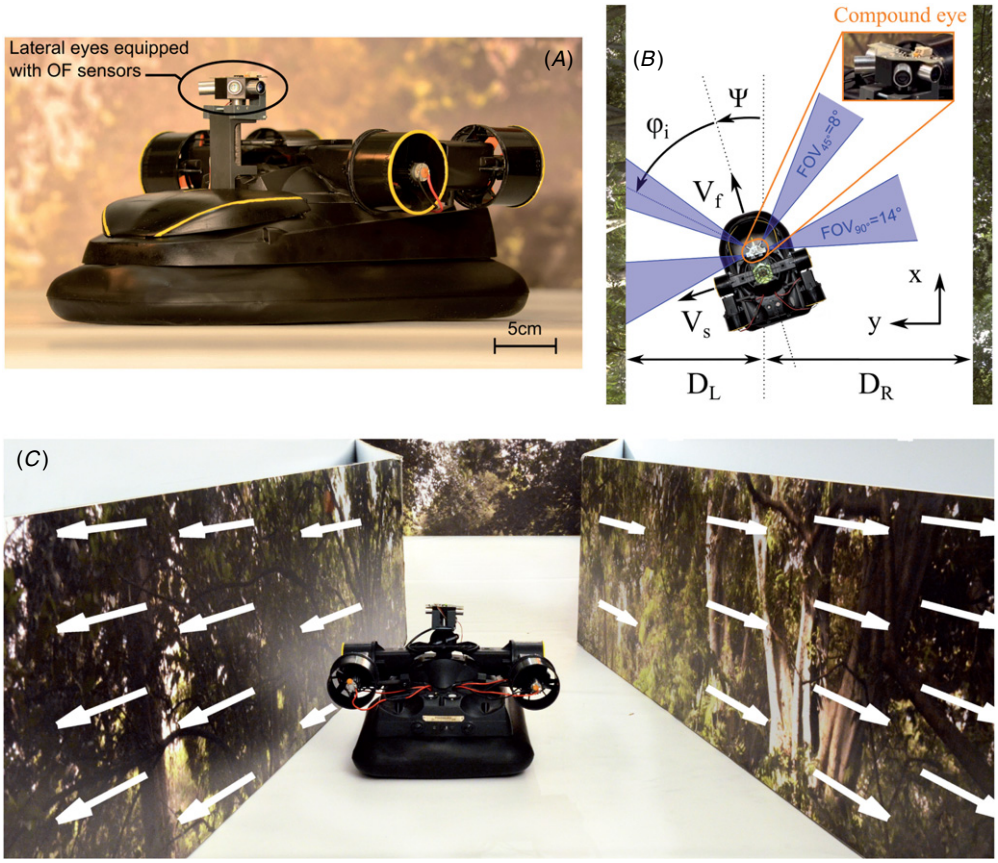

Figure 1. (*A*) A fully autonomous sighted hovercraft equipped with a miniature 8 pixel compound eye. (*B*) Tiny hovercraft (size: $0.36 \times 0.21 \times 0.17$ m^3; mass: 0.87 kg) navigating along an unknown textured corridor. The robot is *fully actuated* by means of four ducted fans controlling its three degrees of freedom (on the surge, sway and yaw axes). A lift fan inflates the skirt and creates an air cushion a few millimetres high ($\sim$2 mm) under the robot, preventing it from touching the ground. The LORA robot is equipped with an insect-inspired compound eye composed of four lateral eyes, i.e., four fly-inspired 2 pixel local motion sensors (LMSs), placed at $\varphi_i = \pm 45^\circ$ and $\varphi_i = \pm 90^\circ$ azimuthal angles (as shown in the inset) measuring the visual motion. The right and left walls of the corridor are lined with a natural coloured panorama depicting bushes and trees. (*C*) The hovercraft travels along a tapered corridor under purely translational optic flow (OF). This OF experienced by the robot is schematized by the white arrows on the walls.

1.1. Contributions of this paper

This study in the framework of biorobotics, where robots are often used as models for explaining animals behaviour, shows that bees' behaviour can be modelled on the basis of OF measurements when they are flying along corridors with various configurations. The responses of this model to the uncertainties inherent to real environments, real actuators and real sensors were tested by implementing it onboard a real robotic demonstrator (a fully autonomous hovercraft). The hovercraft's visually guided animal behaviour was therefore tested in corridors with various configurations (including corridors with stiffly tapering angles, bent corridors and straight stationary corridors placed on a flat or sloping terrain) lined with a natural coloured panorama depicting bushes and trees. Sloping terrain affected the hovercraft's speed in the same way as head or tail wind disturbances. In addition, the corridor was equipped with a moving wall to test the robot's reaction to various unilateral OF perturbations. In a nutshell, this study is the first systematic comparison between the visual guidance performances of a biomimetic robot and those of bees. The control scheme underlying the hovercraft's behaviour accounts for many of the feats performed by bees, as described by several authors during the last 25 years, whereas previous bio-inspired robots do not account for all these insects performances. Our results will predictably open up new avenues for designing further biological experiments, the results of which should help in turn to improve the model.

2. The LORA hovercraft robot

2.1. Dynamic model and identification of the hovercraft robot

The LORA robot (figure 1(*A*)) is a retro-fitted version of a miniature RC hovercraft (Seguchi and Ohtsuka 2003). The hovercraft's skirt creating an air-cushion underneath the robot is inflated by means of a lift fan actuated by a brushless motor. The hovercraft is *fully actuated* by means of four ducted fans driving it on the horizontal plane and controlling its three degrees of freedom (on the surge, sway and yaw axes, figure 1(*B*)). Each of the four thrusters equipping the LORA robot is composed of a dc motor loaded with a light three-blade propeller producing a thrust of up to 0.72 N at 7.2 V and are controlled thanks to a home-made electronic board (figure 2). As the propellers' profile is asymmetrical, reversing the thrust would not brake the robot but just cause it to slow down.

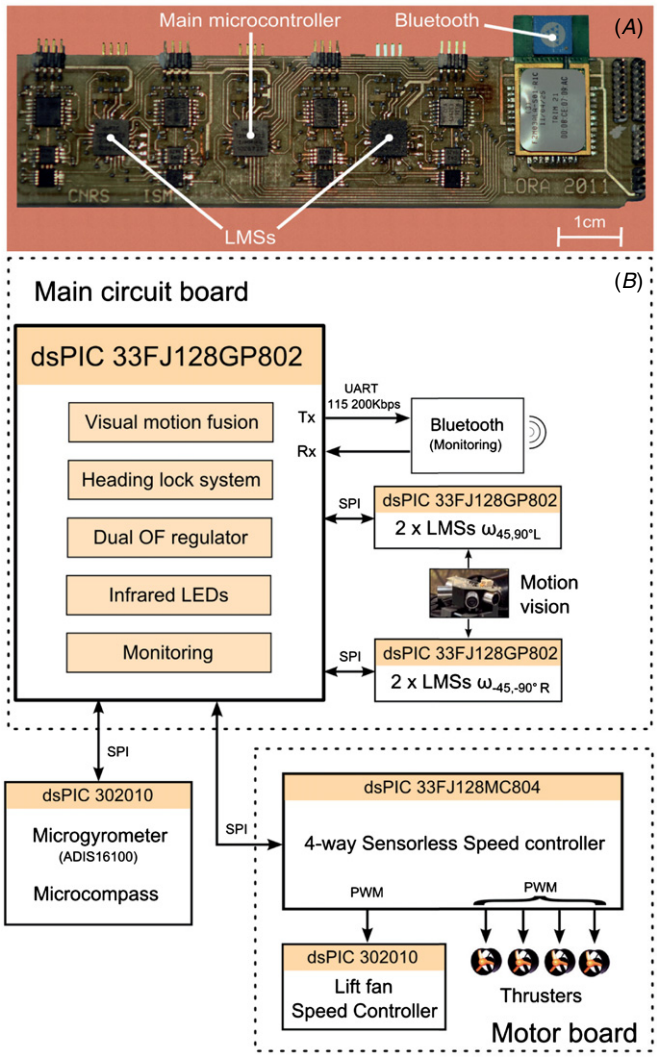

Figure 2. Custom electronics: (*A*) Top view of the microcontroller-based (μC) circuit board (size: 109 × 25 mm^2, mass: 8 g) including the embedded OF-based autopilot and visual LMSs. (*B*) Simplified scheme of the embedded electronics, showing the interconnections between the six tiny μC*s* and the minimalistic 8 pixel compound eye.

The lift fan was therefore used as a 'brake', as suggested in Jin *et al* (2004), by smoothly deflating the skirt. The forward and side dynamics of the hovercraft ($G_{\mathrm{Fwd}}(s)$ and $G_{\mathrm{Side}}(s)$, respectively) corresponding to several lift-fan output signals u_{LiftFan} were identified in the [37%; 42%] range corresponding to the duty cycle of the pulse-width modulation (PWM) signal delivered to the lift-fan controller.

When the hovercraft's heading Ψ is stabilized on the x-axis of the corridor (see section 3.1), the equations of motion along the x- and y-axes can be written as follows:

$$m \cdot \frac{\mathrm{d}V_f}{\mathrm{d}t} + \zeta_f \cdot V_f = 2K_T \cdot U_{\mathrm{batt}} \cdot u_f \tag{1}$$

$$m \cdot \frac{\mathrm{d}V_s}{\mathrm{d}t} + \zeta_s \cdot V_s = K_T \cdot U_{\mathrm{batt}} \cdot u_s, \tag{2}$$

where m (0.878 kg) is the mass, K_T is the identified gain linking the thruster's force to the voltage applied and ζ_f and ζ_s are the forward and lateral linear friction coefficients, respectively. The control signals u_f, u_s and u_Ψ command the surge dynamics (equation (1)), the sway dynamics (equation (2)) and the yaw dynamics, respectively. Each of the four thrusters is controlled by combining the three control signals u_f, u_s and u_Ψ to obtain a PWM signal.

Since the dynamics were identified on a flat terrain ($\beta = 0°$), the forward and side dynamics were expected from equations (1) and (2) to be

$$G_{V_f}(s) = \frac{\frac{2K_T \cdot U_{\mathrm{batt}}}{\zeta_f}}{1 + \frac{m}{\zeta_f} \cdot s} = \frac{K_{\mathrm{Fwd}}}{1 + \tau_{\mathrm{Fwd}} \cdot s} \tag{3}$$

$$G_{V_s}(s) = \frac{\frac{K_T \cdot U_{\mathrm{batt}}}{\zeta_s}}{1 + \frac{m}{\zeta_s} \cdot s} = \frac{K_{\mathrm{Side}}}{1 + \tau_{\mathrm{Side}} \cdot s} \cdot \tag{4}$$

The surge and sway dynamics of the hovercraft ($G_{V_f}(s)$ and $G_{V_s}(s)$, respectively) were therefore identified as a first-order transfer function (equations (3) and (4)), in which the two time constants τ_{Fwd} and τ_{Side} are of the same order of magnitude. Parameters $K_{\mathrm{Fwd,Side}}$ and $\tau_{\mathrm{Fwd,Side}}$ corresponding to each of the control signals u_{LiftFan} are given in tables 2 and 3.

2.2. The bio-inspired robot's visual system

Our hovercraft robot is equipped with a minimalistic compound eye consisting of only four local motion sensors (LMSs), based on 2 pixel OF sensors placed at azimuthal angles of ±45° and ±90° with a horizontal FOV of 8° and 14°, respectively (figure 1(*B*)). Each of the four LMS consists of an optical assembly composed of a lens and a pair of photosensors (based on an iC-LSC photodiode array purchased from the company iC-Haus). An on-chip current amplifier is integrated into each photosensor, but a programmable gain was recently added to the circuit so as to be able to use the maximum range of the analogue-to-digital converter (ADC) of the μC (figure 3) (Ruffier and Expert 2012). When the robot moves straight ahead along a corridor, each eye receives within its small FOV a purely translational OF (figure 1(*C*)), which is defined as follows:

$$\omega_i = \frac{V_f}{D_{\varphi i}} \cdot \sin \varphi_i, \tag{5}$$

where V_f is the robot's forward speed and D_{φ_i} is the distance from an object in the azimuthal direction φ_i. The OF is computed here using the 'time of travel' scheme (figure 3), which gives the angular speed ω_i of any dark-to-light (ON) or light-to-dark (OFF) contrast (as occurs in flies (Franceschini *et al* 1989, Eichner *et al* 2011)), which is determined by measuring the time lag Δt_i between the output signals of two neighbouring photosensors:

$$\Delta t_i = \frac{\Delta \varphi_i}{\omega_i}, \tag{6}$$

where the inter-receptor angle, i.e., the angle between two adjacent photosensors, is denoted by $\Delta\varphi_i$. As also occurs in flies, each photosensor features a Gaussian angular sensitivity function (ASF) (Götz 1964), which is characterized by the acceptance angle $\Delta\rho_i$ (the angle of the ASF at half height).

The latter is tuned here by slightly defocusing the lens from the sensor so as to equalize the values of $\Delta\varphi_i$ and $\Delta\rho_i$ as follows:

$$\Delta\varphi_{90^\circ} = \Delta\rho_{90^\circ} = 3.5^\circ \quad (7)$$

$$\Delta\varphi_{45^\circ} = \Delta\rho_{45^\circ} = 2.5^\circ. \quad (8)$$

Interestingly, the values of the interommatidial angles $\Delta\varphi_{\pm 90^\circ}$ and $\Delta\varphi_{\pm 45^\circ}$ obtained stand comparison with those measured at the same azimuths in the honeybee's compound eye (Seidl 1982). The other processing steps involved in the functional 'time of travel' scheme have been described in detail in previous studies (Blanes 1986, Pichon *et al* 1989, Expert *et al* 2011, Roubieu *et al* 2013). The descending neurons found to exist in honeybees respond monotonically to front-to-back translational movements (VT neurons) (Ibbotson 2001), thus acting like genuine OF sensors. Each of the visual motion sensors implemented in the hovercraft measures the 1D angular speed ω_i^m generated by a natural scene within a range of more than one decade [25° s^{-1}; 350° s^{-1}], which is similar to the visual motion measurement range of VT neurons [40° s^{-1}; 1000° s^{-1}] (Ibbotson 2001).

In the case of the tapered corridor, the translational OF ω_φ experienced by the robot looking at one of the corridor walls at azimuth φ depends on the tapering angle α, and therefore ω_φ can vanish and even make a change of direction. This can be confirmed as follows (in the following equations, the same notation is used as in the figure 1(*B*)):

$$\omega_\varphi = \frac{V_f \sin\varphi - V_s \cos\varphi}{D_\varphi} \quad (9)$$

where $\Psi = 0$ and $\dot{\Psi} = 0$

$$D_\varphi = \frac{D(0^\circ)\cdot(1+\tan^2(\varphi))\cdot\cos\varphi)}{1+(\tan\varphi\cdot\tan(\alpha-\pi/2))} \quad (10)$$

which gives

$$\omega_\varphi = \frac{(V_f\sin\varphi - V_s\cos\varphi)\cdot\sin\varphi}{D(0^\circ)\cdot(1+\tan^2(\varphi))} \cdot(1+(\tan\varphi\cdot\tan(\alpha-\pi/2))). \quad (11)$$

The sign of ω_φ therefore depends on the sign of $1-\frac{\tan\varphi}{\tan\alpha}$ and on that of $V_f\sin\varphi - V_s\cos\varphi$.

In the present case, the orientation of the OF sensors φ (45° or 90°) is always greater than the tapering angle α (7° or 14°). This means that the direction of the OF will change only if the angle of orientation of the speed vector becomes greater than that of the OF sensors (45° or 90°). Thanks to our heading-lock system and our dual OF regulator, the robot always followed the wall in the steady state and the orientation of the robot's speed vector was always approximately equal to the value of the tapering angle (i.e., about 7° or 14°) as established in previous computer simulations (Serres *et al* 2008a)). It is most unlikely that the direction of the OF might change in the case of OF sensors oriented at 45° or 90°.

2.3. Hardware architecture

The photograph of the main electronic board presented in figure 2(*A*) shows the three microcontrollers (μCs—dsPic33FJ128GP802 from Microchip©) responsible for the visual signal processing and the OF-based visuomotor feedback loops guiding the LORA robot. The block diagram presented in figure 2(*B*) shows the architecture of the electronic system integrated into the LORA robot. The main μC deals with multi-rate tasks such as the heading-lock control system, the visual motion fusion process feeding the *dual OF regulator*, the data monitoring performed during the main tasks and the supervision of the two secondary μCs responsible for the lateral OF processing. The main dsPIC therefore fuses the visual inputs (i.e., the OF measurements $\omega_{\varphi_i}^m$), the inertial input (i.e., the rate gyro $\dot{\Psi}^m$) and the vehicle's heading (i.e., the custom micro-magnetic compass Ψ^m). A bluetooth device connected to the UART peripheral of the main μC provides a full-duplex radio link between the freely moving robot and the ground station so that the hovercraft's data can be remotely monitored and instructions (as regards the values of the OF-set-points, for instance) can be delivered. Two separate Li–polymer battery packs for the motors and the electronics (7.2 V, 2200 mAh and 7.2 V, 360 mAh, respectively) give the robot an endurance of 10 min. Robustness to large voltage disturbances was provided by a four-way 'sensorless speed governor' (Viollet *et al* 2008) controlling the four propellers' rotational speeds (*rpm*) in the closed-loop mode, whereas the lift-fan *rpm* was controlled via an optical sensor. The hovercraft is fully autonomous without requiring any umbilical links: it performs all the processing steps onboard and carries all its own sensors and actuators, its own wireless data link and its own power supplies. To summarize, the 6 μCs distributed in the LORA robot (figure 2(*B*)) handle no less than eight feedback loops (including the four sensorless speed governors) and make the robot relatively immune to heading disturbances and power supply variations.

3. The bee-inspired LORA autopilot

The autopilot embedded onboard the real hovercraft (figure 1) performs multiple data-processing stages, as shown in figure 4. In addition to the bio-inspired *dual OF regulator*, the heading-lock system was introduced to make the robot move straight ahead along the corridor axis. The autopilot therefore controls the robot's motion not only forward and sideways, but also about the yaw axis, in line with the principles described in this section.

3.1. The heading-lock system

The hovercraft's heading Ψ is stabilized along the main axis of the corridor (the *x*-axis) via the heading-lock system based on a micro-gyro and a micro-magnetic compass (figure 4(*A*)), which compensates for any yaw disturbances by adjusting the rear thrusters *differentially*. The robot therefore experiences a purely *translational* OF (figure 1(*C*)), as defined in equation (5).

The heading feedback loop, which is composed of two nested feedback loops, nullifies the robot's yaw speed and angle ($\dot{\Psi} = 0^\circ$ s^{-1} and $\Psi = 0^\circ$) in order to cancel any yaw drift. A proportional controller $C_\Psi(s)$ was included in the outer feedback loop (based on the magnetic micro-compass $H_c(s)$) and a proportional-integral (PI)

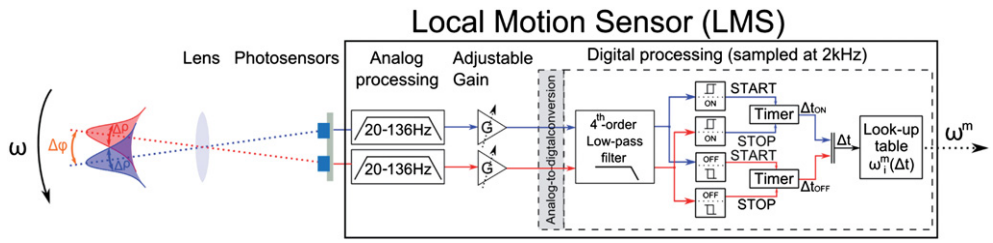

Figure 3. Processing architecture of one 2 pixel local motion sensor (LMS). The visual signals delivered by neighbouring photosensors are filtered both spatially and temporally by an analogue bandpass filter with cut-off frequencies of 20 Hz and 136 Hz and a second-order fixed-point digital low-pass filter with a cut-off frequency of 30 Hz. The visual signals are then amplified before being digitized using the programmable gain controlled by an SPI bus in order to finely tune the dynamic range of the signals to the ambient illuminance and use the maximum range of the analogue to digital converter (Ruffier and Expert 2012). The filtered photosensor signals are then thresholded to determine the angular speed ω^m, using the 'time of travel' scheme previously developed at our laboratory (Blanes 1986, 1991, Pichon *et al* 1989, Franceschini *et al* 2009). The 'time of travel' Δt, which is proportional to the inverse of ω, elapsing between two filtered photosensor signals is measured by a timer: Δt_{ON} and Δt_{OFF} are measured by means of ON and OFF contrast distinguishing processes inspired by the fly's eye (Franceschini *et al* 1989). The delay Δt is measured and then used to compute the 1D angular speed ω^m in the local visual field. The overall processing was carried out on a tiny low-power 16 bit μC (dsPIC33F128GP802 from Microchip©) at a sampling rate of 2kHz, giving a 0.5 ms precision measurement in the Δt measurement range. Whenever an LMS does not detect any new contrasting features, it holds the last measured value for a period of 0.5 s. Modified from Ruffier and Expert (2012).

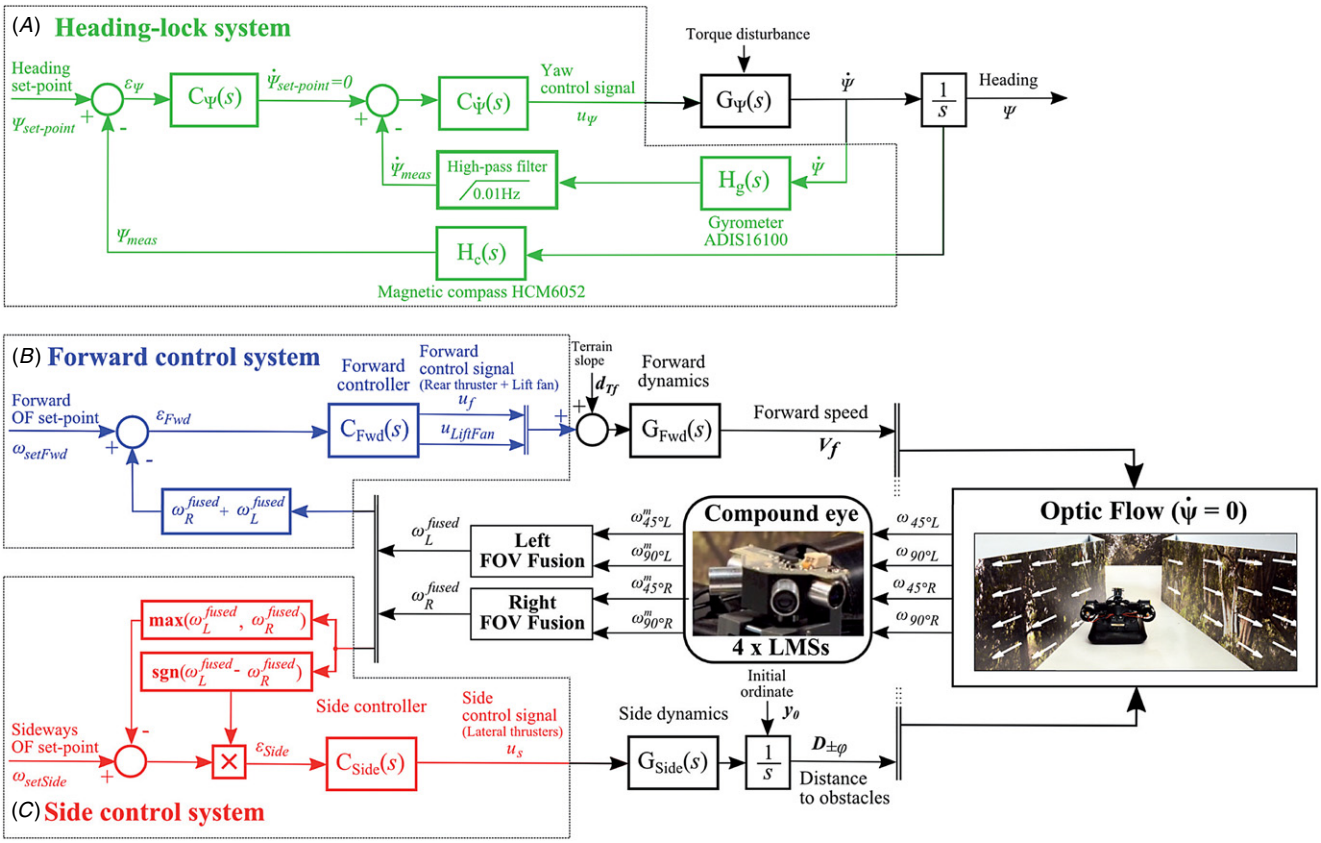

Figure 4. Feedback loops implemented on the robot. (*A*) Custom-made heading-lock system composed of a micro-gyrometer and a micro-compass compensating for any yaw disturbances and keeping the robot's heading on the *x*-axis of the corridor ($\Psi = 0°$—figure 1(*B*)). (*B*) and (*C*) The bio-inspired OF-based autopilot consists of a *dual lateral OF regulator* based on two interdependent visuomotor feedback loops: a forward control loop and a side control loop, each of which has its own OF set-point, that is, ω_{setFwd} and ω_{setSide}. The forward control system (*B*) is a *bilateral* OF regulator that adjusts the forward thrust and the lift-fan control signal so as to keep the sum of the right and left fused OF $\omega_R^{\text{fused}} + \omega_L^{\text{fused}}$ constant at ω_{setFwd}. The side control system (*C*) adjusts the lateral thrust on the basis of whichever of the two fused lateral OFs measured is the larger: $\max(\omega_R^{\text{fused}}, \omega_L^{\text{fused}})$. Details of each transfer function and their parameters are given in tables 1, 2 and 3.

controller $C_{\dot{\psi}}(s)$ was integrated into the inner-feedback loop (based on the micro-gyrometer $H_g(s)$) to improve the closed-loop dynamics and obtain a zero steady-state error, thus locking the robot's heading to the *x*-axis of the corridor (see figures 1(*B*) and 4(*A*)).

3.2. The bio-inspired dual lateral optic flow regulation

The *dual lateral OF regulator* consists of two intertwined visuomotor feedback loops controlling both the forward and sideways motion of the robot on the basis of the OF (figures 4(*B*) and (*C*)).

The robot's side control system previously tested in computer simulations Serres *et al* 2008a) was initially inspired by our findings obtained on honeybees' wall-following behaviour (Serres *et al* 2008b) and on previous findings obtained on bees' centring behaviour (Kirchner and Srinivasan 1989). An explicit control system called the *side control feedback loop* shown in figure 4(*C*) (red loop) was developed. This first lateral OF regulator is a *unilateral* OF regulator that adjusts the vehicle's lateral thrust (which determines the sway speed V_s) so as to keep the higher of the two fused lateral OFs perceived, that is, $\max\left(\omega_{R,L}^{\text{fused}}\right)$, equal to the *sideways OF set-point* ω_{setSide}. The sign function $sgn(\omega_L^{\text{fused}} - \omega_R^{\text{fused}})$ selects the direction corresponding to the nearest wall $\min(D_{L,R})$, i.e., the wall generating the greatest lateral OF. Thanks to this unilateral OF regulator, the distance from this wall becomes automatically proportional to the robot's forward speed V_f, whatever the speed or the distance involved. The faster the robot travels, the further away from that wall it will therefore be. The clearance from the walls ($D_{L,R}$) depends mainly on the *sideways OF set-point*. A lead integrator $C_{\text{Side}}(s)$ was introduced into the side feedback loop to increase the damping, thus improving the robot's stability and its sway dynamics. The error signal ϵ_{Side} is calculated as follows:

$$\epsilon_{\text{Side}} = sgn\left(\omega_L^{\text{fused}} - \omega_R^{\text{fused}}\right) \times \left[\omega_{\text{setSide}} - \max\left(\omega_{R,L}^{\text{fused}}\right)\right]. \quad (12)$$

Only one lateral thruster is actuated at a time, depending on the sign of the output control signals u_s delivered by the side controller:

- $u_s < 0$: the left thruster is actuated and the right one is off and
- $u_s > 0$: the right thruster is actuated and the left one is off.

The robot's forward control system, which was previously tested in computer simulations, was based on findings obtained on the flight behaviour of honeybees in a narrow tapered corridor lined with a periodic pattern of black and white vertical stripes (Srinivasan *et al* 1996). The forward control system is provided here by the second OF regulator (figure 4(*B*), blue loop), which holds the sum of the two fused lateral OFs measured, that is $\omega_L^{\text{fused}} + \omega_R^{\text{fused}}$, constant and equal to the forward OF set-point ω_{setFwd}. At all times, it adjusts the forward thrust, which will determine the hovercraft's forward speed V_f. At a given corridor width, any increase in the sum of the two lateral OFs is assumed here to result from the hovercraft's acceleration. This control scheme thus automatically ensures a 'safe forward speed' which is commensurate with the local corridor width without requiring any information at all about the width of the corridor. A PI controller $C_{\text{Fwd}}(s)$ was introduced into the forward feedback loop to improve the closed-loop dynamics and obtain a zero steady-state error, and therefore to reject any disturbances d_{Tf} (equation (17)) due to the sloping terrain. The error signal ϵ_{Fwd} feeding the forward controller is calculated as follows:

$$\epsilon_{\text{Fwd}} = \omega_{\text{setFwd}} - \left(\omega_L^{\text{fused}} + \omega_R^{\text{fused}}\right). \quad (13)$$

Our control method enables the robot to control its forward speed V_f smoothly by combining the rear thrusters' and lift-fan control signals (u_f and u_{LiftFan}, respectively) in the same forward controller. Depending on the sign of the output control signal produced by the forward controller u_f, the robot can therefore:

- speed up ($u_f > 0$) by boosting the rear thrusters in the [0%; 60%] range (PWM) and u_{LiftFan} to the maximum value of 42%;
- slow down ($u_f = 0$) by switching off the rear thrusters and keeping u_{LiftFan} at the maximum value of 42% and
- 'brake' ($u_f < 0$) by switching off the rear thrusters and deflating the skirt via u_{LiftFan} in the identified [37%; 42%] range.

Table 1. Transfer functions in figure 4.

Transfer functions	Parameters value
$H_c(s) = K_c$	With $K_c = 9.17 \times 10^{-3}$ V/°
$H_g(s) = K_g$	With $K_g = 5 \times 10^{-3}$ V/(°/s)
$G_\Psi(s) = \frac{1}{s} \cdot \frac{H_\Psi}{1+\tau_\Psi \cdot s}$	With $H_\Psi = 4.4 \times 10^{-1}$ V and $\tau_\Psi = 3 \times 10^{-1}$ s
$G_{\text{Fwd}}(s) = \frac{K_{\text{Fwd}}}{1+\tau_{\text{Fwd}} \cdot s}$	See values in table 2
$G_{\text{Side}}(s) = \frac{K_{\text{Side}}}{1+\tau_{\text{Side}} \cdot s}$	See values in table 3
$C_\Psi(s) = K_\Psi$	With $K_\Psi = 3$
$C_\Psi(s) = K_1 \cdot \frac{1+\tau_1 \cdot s}{s}$	With $K_1 = 5$ and $\tau_1 = 3 \times 10^{-1}$ s
$C_{\text{Fwd}}(s) = K_2 \cdot \frac{1+\tau_2 \cdot s}{s} \cdot \frac{1}{1+\tau_3 \cdot s}$	With $K_2 = 0.8$, $\tau_2 = 2.7 \times 10^{-1}$ s and $\tau_3 = 8 \times 10^{-3}$ s
$C_{\text{Side}}(s) = K_3 \cdot \frac{1+a \cdot T \cdot s}{1+T \cdot s} \cdot \frac{1}{1+\tau_4 \cdot s}$	With $K_3 = 4 \times 10^{-1}$, $a = 5.7$, $T = 2.1 \times 10^{-1}$ and $\tau_4 = 1.59 \times 10^{-2}$ s

The three feedback loops that make up the heading-lock system and the *dual OF regulator* are implemented in parallel on the main μC of the main circuit board (figure 2(*A*)) and control the LORA robot at a sampling frequency of 100 Hz. All the transfer functions presented in this section are presented in detail in table 1.

Once the OF-based autopilot has reached the steady state ($V_{f\infty}$, $D_{R,L\infty}$), the LORA robot will travel at a given forward speed $V_{f\infty}$ and at a given distance from one wall ($D_{L\infty}$ or $D_{R\infty}$). The steady-state operating point depends on the two OF set-points ω_{setFwd} and ω_{setSide}, as shown in figure 5(*A*) in the case of wall-following behaviour and by figure 5 B in that of centring behaviour.

3.3. Visual motion fusion

Two versions of a minimalistic bee-inspired compound eye were implemented on the hovercraft equipped with the *dual OF regulator*. We first tested the performances of this autopilot with a 4 pixel compound eye consisting simply of two pairs of pixels (±90° azimuthal angles) and then extended the visual field towards the front by adding two pairs of pixels in the ±45° optical directions, giving an 8 pixel compound eye. We therefore needed to feed the autopilot with a combination of these four visual motion signals. The visual fusion method defined below describes the contents of the 'left or right FOV fusion' blocks presented in figure 4.

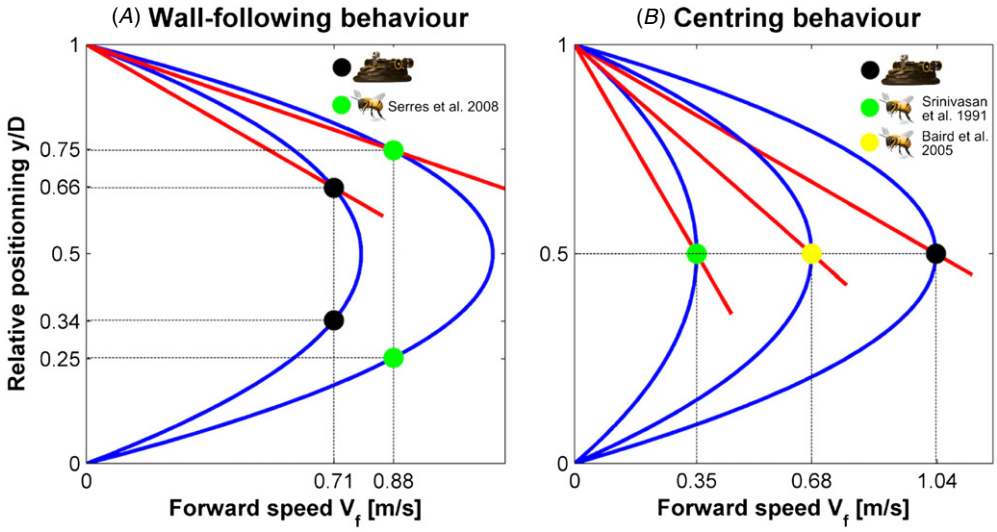

Figure 5. Comparison between robot and bees' operating points, assuming that bees' behaviours are consistent with our dual optic flow regulator model depending on both ω_{setFwd} and ω_{setSide}. The blue parabola represents the set of operating points for which the bilateral optic flow is constant at a given corridor width D. The red straight line represents the set of operating points for which the unilateral optic flow (here, left) is constant at a given corridor width D. To compare several operating points on a same graph at different corridor widths D, the lateral positioning is normalized by the corridor width y/D. (*A*) Wall-following behaviour: $2 \cdot \omega_{\text{setSide}} < \omega_{\text{setFwd}}$. Black operating points for the LORA robot with $\omega_{\text{setFwd}} = 190^\circ\ \text{s}^{-1}$ and $\omega_{\text{setSide}} = 125^\circ\ \text{s}^{-1}$ with $D = 0.92$ m. Green operating points for bees with $\omega_{\text{setFwd}} = 281^\circ\ \text{s}^{-1}$ and $\omega_{\text{setSide}} = 210^\circ\ \text{s}^{-1}$ with $D = 0.95$ m given $D_{R,L\infty} = 0.24$ m and $V_{f\infty} = 0.88\ \text{m s}^{-1}$, as observed in Serres *et al* (2008b). (*B*) Centring behaviour: $2 \cdot \omega_{\text{setSide}} \geqslant \omega_{\text{setFwd}}$. Black operating point for the LORA robot with $\omega_{\text{setFwd}} = 250^\circ$ s and $\omega_{\text{setSide}} = 125^\circ$ s with $D = 0.92$ m. Green operating point for bees with $\omega_{\text{setFwd}} = 668^\circ$ s and $\omega_{\text{setSide}} = 334^\circ$ s with $D = 0.12$ m given $D_{R,L\infty} = 0.06$ m and $V_{f\infty} = 0.35\ \text{m s}^{-1}$ as observed in Srinivasan *et al* (1991), and yellow operating point with $\omega_{\text{setFwd}} = 488^\circ\ \text{s}^{-1}$ and $\omega_{\text{setSide}} = 244^\circ\ \text{s}^{-1}$ with $D = 0.32$ m given $D_{R,L\infty} = 0.16$ m and $V_{f\infty} = 0.68\ \text{m s}^{-1}$ as observed in Baird *et al* (2005).

3.3.1. The case of a compound eye consisting of two pairs of pixels. Using only the $\pm 90^\circ$ lateral eyes, we have:

$$\omega_{L,R}^{\text{fused}} = \omega_{\pm 90^\circ}^{m}. \tag{14}$$

3.3.2. The case of a compound eye consisting of four pairs of pixels. The four LMSs output signals are combined to generate the ω_L^{fused} and ω_R^{fused} visual signals by taking the maximum value of each weighted OF output signal according to the following equation:

$$\omega_{R,L}^{\text{fused}} = \max(K_{-\varphi_i,\varphi_i} \cdot \omega_{-\varphi_i,\varphi_i}) \tag{15}$$

with the gain K_{φ_i} computed as follows:

$$K_{\varphi_i} = \frac{1}{\sin^2 \varphi_i}. \tag{16}$$

4. Experimental results obtained with a 4 pixel compound eye

In this section, we describe the performances of the hovercraft travelling along challenging unknown corridors (figures 6–12), thanks to the *dual OF regulator* and its bee-inspired compound eye consisting of just two pairs of pixels. When entering these corridors, the LORA robot was never provided with any explicit information about either its current forward speed V_f, its current distance from the walls D_R or D_L, or any other details about the corridors configuration. The experiments were carried out indoors under artificial lighting conditions. The visual motion fusion method presented in equation (14) was used to generate the right and left visual motion measurements $\omega_{R,L}^{\text{fused}}$ feeding the autopilot (figure 4). In each experiment presented in this section, the OF set-points of the vision-based autopilot were fixed at $\omega_{\text{setFwd}} = 190^\circ\ \text{s}^{-1}$ and $\omega_{\text{setSide}} = 125^\circ\ \text{s}^{-1}$.

A digital camera (a Fastec Imaging TroubleShooter) was used to record the robot's trajectories. All the details of the offline processing of the LORA robot's trajectory can be found in Roubieu *et al* (2012).

4.1. Wall-following and centring behaviours in both straight and tapered corridors

In figure 7, the hovercraft entered the straight corridor on a central course (see the 3D trajectory in figure 7(*B*)). The trajectory plotted here shows that the robot glided safely at a constant clearance from the nearest wall ($D_{L,R\infty} = 0.31$ m, grey dash–dotted line), i.e., that nearest to the starting point. This means that the *sign* function ($sgn(\omega_L^{\text{fused}} - \omega_R^{\text{fused}})$, figure 4(*C*)) selected the direction towards the nearest wall and the criterion $\max(\omega_{R,L}^{\text{fused}})$ sent the corresponding LMS output to the autopilot (left $+90^\circ$ LMS in figure 7(*E*), red dotted line). The speed profile shows that the hovercraft kept an appropriate 'cruise' speed of $V_{f\infty} = 0.69\ \text{m s}^{-1}$ (figure 7(*D*)). The forward OF regulator therefore strived to maintain the sum of the two measured lateral OFs, that is, $\Sigma\omega_{R,L}^{\text{fused}}$ (figure 7(*E*), blue dash–dotted line), at a constant value corresponding to the forward OF set-point ω_{setFwd}. The hovercraft therefore adopted *wall-following* behaviour and kept its speed constant, in line with the constant local

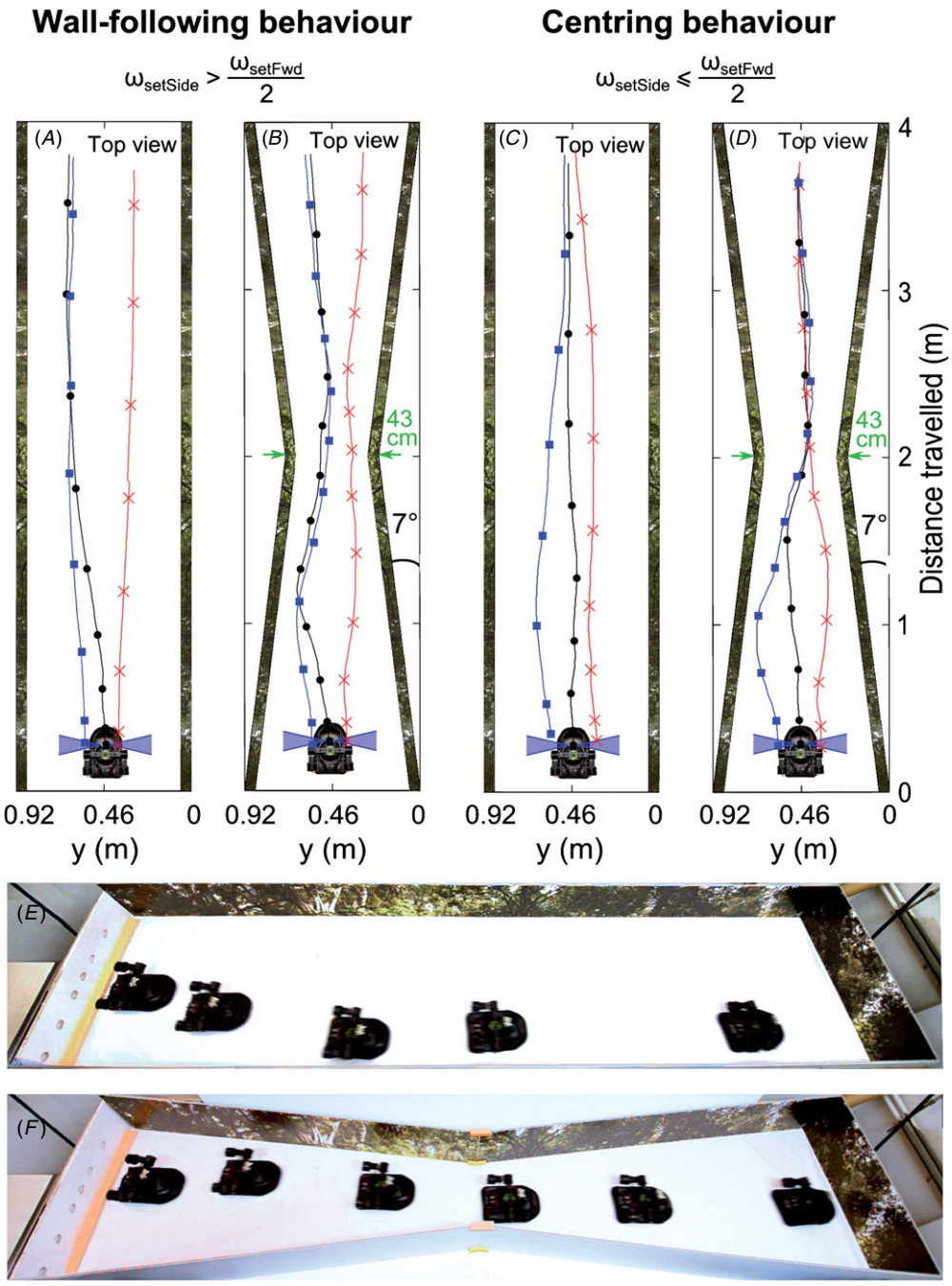

Figure 6. Automatic speed control and lateral positioning of a miniature *fully actuated* hovercraft navigating in a 4 m long straight or tapered corridor. The hovercraft embeds the bee-inspired LORA autopilot based on the *dual OF regulators* and is endowed with an insect-inspired 4-pixel visual system. The robot performs either a *wall-following* ((*A*) and (*B*)) or a *centring* behaviour ((*C*) and (*D*)) which depends only on the set of OF set-points with $\omega_{setFwd} = 250^\circ\ s^{-1}$ and $\omega_{setSide} = 125^\circ\ s^{-1}$ for the *centring* behaviour, i.e., here $\omega_{setSide} \leqslant \frac{\omega_{setFwd}}{2}$, as well as with $\omega_{setFwd} = 250^\circ\ s^{-1}$ and $\omega_{setSide} = 160^\circ\ s^{-1}$ for the *wall-following* behaviour, i.e. $\omega_{setSide} > \frac{\omega_{setFwd}}{2}$. The autonomous LORA robot entered the corridor without being informed about the configuration of the corridor and therefore operated in (*E*) a *wall-following* behaviour (1.12 s time interval chronophotography—black trajectory in (*A*)) and a *centring* behaviour in (*F*) (1.33 s time interval chronophotography—black trajectory in (*D*)). See video www.dailymotion.com/embed/video/xuggrs.

corridor width. Upon applying these tests with various OF set-points (figure 6), it was observed that it is possible for the hovercraft equipped with the *dual OF regulator* to perform either *wall-following* behaviour ($\omega_{setFwd} = 250^\circ\ s^{-1}$ and $\omega_{setSide} = 160^\circ\ s^{-1}$; figure 6(*A*)) or *centring* behaviour ($\omega_{setFwd} = 250^\circ\ s^{-1}$ and $\omega_{setSide} = 125^\circ\ s^{-1}$; figure 6(*C*)), after taking several starting points. In each case, the marks on the trajectories plotted show that the robot kept a virtually constant 'cruise' speed while travelling along the corridor. These results show that the dual OF regulator accounts not only for bees' *wall-following* behaviour—which will be observed whenever $\omega_{setSide} > \frac{\omega_{setFwd}}{2}$—but also for their centring behaviour, which will be observed whenever $\omega_{setSide} \leqslant \frac{\omega_{setFwd}}{2}$. The only condition which must be met to obtain either

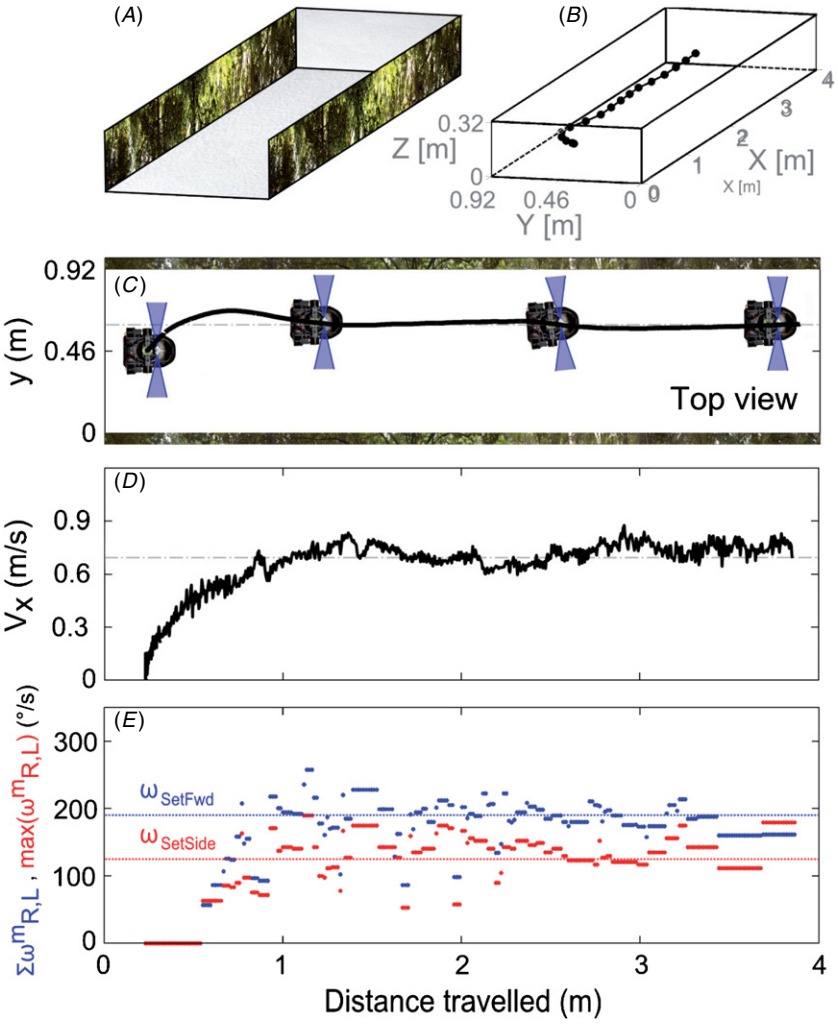

Figure 7. Automatic *wall-following* behaviour of the LORA robot in a straight 4 m long corridor. The robot was equipped with a 4 pixel compound eye facing in ±90° optical directions. (FOVs are presented in the form of blue conical shapes.) The LORA robot started on a central course ($x_0 = 0.25$ m and $y_0 = 0.46$ m) with $\omega_{\text{setFwd}} = 190^\circ\ \text{s}^{-1}$ and $\omega_{\text{setSide}} = 125^\circ\ \text{s}^{-1}$ OF set-points. (*A*) Perspective view of the straight corridor. (*B*) 3D trajectory of the hovercraft robot navigating along the straight corridor plotted every 0.4 s. (*C*) Chronophotograph of the hovercraft robot in the horizontal plane. Marks on the trajectory indicate the robot's position and orientation at 2.17 s time intervals. In the steady state, the clearance from the nearest wall reached $D_{L\infty} = 0.31$ m, and the robot performed safe *wall-following* behaviour. (*D*) Forward speed profile V_f corresponding to the trajectory shown in (*C*). The robot reached a steady-state forward speed ($V_{f\infty} = 0.69$ m s^{-1}. (*E*) Forward feedback signal $\Sigma(\omega_{R,L}^{\text{fused}})$ and positioning feedback signal $\max(\omega_{R,L}^{\text{fused}})$ with their respective set-points ω_{setFwd} and ω_{setSide}. The *dual OF regulator* strived to maintain the maximum $\max(\omega_{R,L}^{\text{fused}})$ value and the sum of the two lateral OF $\max(\omega_{R,L}^{\text{fused}})$ at their respective set-points ω_{setSide} and ω_{setFwd}, respectively, thus making the robot perform *wall-following* behaviour.

wall-following or centring behaviour is that the following criterion $\omega_{\text{setSide}} > \frac{\omega_{\text{setFwd}}}{2}$ or $\omega_{\text{setSide}} \leqslant \frac{\omega_{\text{setFwd}}}{2}$ must be respectively satisfied.

The tapered corridors (with tapering angles of 7° and 14°, see figures 10(*A*) and 10(*B*)) were built to test the vision-based autopilot's ability to overcome the *bilateral* OF disturbances introduced by the narrowing walls. Figure 9 shows the trajectory of the LORA robot in a 7° tapered corridor, after being made to take a central course at the start (see the 3D trajectory in figure 9(*B*)). The chronophotograph of the LORA robot (figure 9(*C*)) and the robot's speed profile (figure 9(*D*)) show the robot's response to the 'non-constant OF disturbance': it slowed down *linearly* when approaching the narrowest point and speeded up *linearly* when the corridor widened out beyond that point (figure 9(*D*)). The dual OF regulator controlled the forward speed depending on the local width of the corridor (the predicted speed profile is plotted as a function of *D* in the form of a grey dash–dotted line in figure 9(*D*)). The LORA autopilot therefore easily overcomes the OF disturbance induced by the narrowing walls by modifying its forward speed at all times in keeping with the local corridor width. As can be seen from the tests performed with other starting positions y_0 shown in figure 10(*D*), the robot performed these *wall-following* tests successfully and hugged either the right or left wall, depending on the sign of ϵ_{Side}. The trajectories plotted in figure 10(*D*) show that disturbances of this kind are rejected efficiently by the *dual OF regulator*.

We then tested the hovercraft's ability to navigate along a 7° tapered corridor, taking several pairs of OF set-points with

($\omega_{\text{setFwd}} = 250^\circ\ \text{s}^{-1}$; $\omega_{\text{setSide}} = 160^\circ\ \text{s}^{-1}$) in figure 6(B)) and ($\omega_{\text{setFwd}} = 250^\circ\ \text{s}^{-1}$; $\omega_{\text{setSide}} = 125^\circ\ \text{s}^{-1}$) in figure 6(*D*). The results obtained showed that the dual OF regulator makes the robot adopt appropriate behaviour, that is, either wall-following behaviour (figure 6(*B*)) or centring behaviour (figure 6(*D*)), depending on the pair of OF set-points chosen. In all cases, the LORA robot adjusted its speed depending on the local corridor width, which is consistent with findings made on honeybees in a similar situation (Srinivasan *et al* 1996).

A more 'challenging' unilateral tapered corridor (with a tapering angle of 14°, figure 10(*B*) generating a stronger OF disturbance than the 7° tapered corridor was also used to test the navigation skills of the LORA robot. The results of the tests conducted in this corridor with several starting positions y_0 (figure 10(*E*)) show that the hovercraft followed either the right or left wall safely (figure 10(*E*)), depending on its initial ordinate y_0. One exception was observed in the case of the initial ordinate $y_0 = 0.16$ m (the green trajectory in figure 10(*E*)), where the robot crashed into the right wall because it started off too close to that wall. This incident shows up the main limitation of using only ±90° lateral eyes, as they did not enable the robot to avoid this lateral obstacle. However, with all the other starting points, the LORA autopilot made the hovercraft travel safely along the 14° tapered corridors without being greatly perturbed by the major OF disturbance induced by the narrowing of the walls, regardless of the starting position y_0 (figures 10(*D*) and 10(*E*)). The robot consistently showed suitable *wall-following* behaviour by following either the left or right wall.

The present findings on robotic navigation along straight and tapered corridors show that the dual OF regulator accounts not only for the centring behaviour (Kircher and Srinivasan 1989, Srinivasan *et al* 1991) and wall-following behaviour (Serres *et al* 2008b) but also for the system of speed control observed in bees in similar situations (Srinivasan *et al* 1996, Baird *et al* 2005, Portelli *et al* 2011).

4.2. Automatic wall-following and centring behaviour in corridors with a sloping floor

We constructed two other straight corridors placed on either an ascending terrain ($\beta = -1^\circ$, figure 8(*A*)) or a descending terrain ($\beta = +1^\circ$, figure 8(*C*)).

The straight corridors with a sloping floor were designed to test the ability of the *dual OF regulators* to cope with a *physical disturbance* d_{Tf} (equation (17), figure 4(*B*)) due to sloping terrain:

$$d_{Tf} = \frac{m \cdot g \cdot \beta}{2K_T \cdot U_{\text{batt}}}. \tag{17}$$

The slope $\beta = -1^\circ$ can be said to be equivalent to the speed disturbance caused by a virtual head wind $V_{\text{wind}_{\text{equivalent}}}$ of $-0.44\ \text{m s}^{-1}$, as described by the following equation:

$$V_{\text{wind}_{\text{equivalent}}} = \tau_f \cdot g \cdot \sin(\beta). \tag{18}$$

In figure 8, the hovercraft is presented as it entered the two straight corridors at $x_0 = 0.25$ m and $y_0 = 0.46$ m (see the 3D trajectories shown in figures 8(*Ab*) and (*Bb*)). The robot showed similar *wall-following* behaviour in a straight corridor placed on a sloping terrain ($\beta = \pm 1^\circ$, figures 8(*Ac*) and (*Bc*)) to that observed when it was flying over a flat terrain ($\beta = 0^\circ$, figure 7(*C*)). Despite the physical disturbance d_{Tf}, the robot kept a constant clearance from the nearest wall ($D_{L,R\infty} = 0.31$ m; figures 8(*Ac*) and (*Bc*)) and a constant 'cruise' speed ($V_{f\infty} = 0.69\ \text{m s}^{-1}$; figures 8(*Ad*) and (Bd)). This steady-state behaviour corresponds to that which can be expected to occur with the pair of OF set-points $\omega_{\text{setFwd}} = 190^\circ\ \text{s}^{-1}$ and $\omega_{\text{setSide}} = 125^\circ\ \text{s}^{-1}$ (figure 5(*A*)). The *dual OF regulator* therefore compensated efficiently for the physical disturbance d_{Tf} (equation (17)) due to the sloping terrain, which was equivalent to that induced by wind (equation (18)).

By setting the pair of OF set-points $\omega_{\text{setFwd}} = 190^\circ\ \text{s}^{-1}$ and $\omega_{\text{setSide}} = 80^\circ\ \text{s}^{-1}$ (figure 5(*B*)) appropriately, the hovercraft automatically centred and maintained its ground speed in the corridor (figures 8(*Cc*) and (*Cd*) and (*Dc*) and (*Dd*)): the robot rejected the physical disturbance due to the positive or negative slope, which had similar effects to those of a positive or a negative speed disturbance.

The present findings on robotic navigation in the presence of speed disturbances show that the principles on which the present dual OF regulator was based also account for bees' centring behaviour in the presence of wind (Barron and Srinivasan 2006).

4.3. Automatic reaction to a 4 m 'no contrast zone' on one of the corridor walls

Tests were then carried out on a 4 m long straight corridor (figure 11(*A*)) and a tapered corridor (with tapering angles of 7° and 14°, see figures 11(*B*) and (*C*)) in which the left wall was lined with a natural coloured panorama. The right wall was devoid of texture, and therefore mimicked the effect of a 4 m 'aperture'. Only the left 2 pixel LMS could provide the autopilot with visual motion cues. These corridor configurations were used to test the behaviour of the LORA robot in the presence of a 'no contrast' zone on one corridor wall and its ability to cope with strong OF disturbances (in the 7° and 14° tapered corridors), although only a single pair of pixels in its visual system received the relevant optical stimuli.

The results obtained with several starting points in a 4 m long straight corridor are shown in figure 11(*A*) and those obtained in tapered corridors with tapering angles of 7° and 14° are shown in figures 11(*B*) and 11(*C*). In the straight corridor configuration, the LORA robot hugged the left wall, i.e., the textured wall, and showed 'wall-following' behaviour even in the 4 m section, where no texture was present on the right wall (figure 11(*D*)), as observed with honeybees in Serres *et al* (2008b). The robot did not rush into the aperture because the positioning criterion selected the left 2 pixel LMS and the *sign* function ($sgn(\omega_L^{\text{fused}} - \omega_R^{\text{fused}})$, figure 4(*C*)) selected the leftward direction that of the textured wall to be hugged. The marks on the trajectories plotted show that the robot accelerated during its journey along the corridor. As the environment was less cluttered in the absence of texture on one wall, the *bilateral* OF regulator made the robot speed up (with $u_{\text{f max}} = 60\%$ and $u_{\text{liftfan}} = 42\%$) until reaching its maximum speed limit $V_{\text{f max}}$ as it could not nullify ϵ_{Fwd}. Based on the forward dynamics of

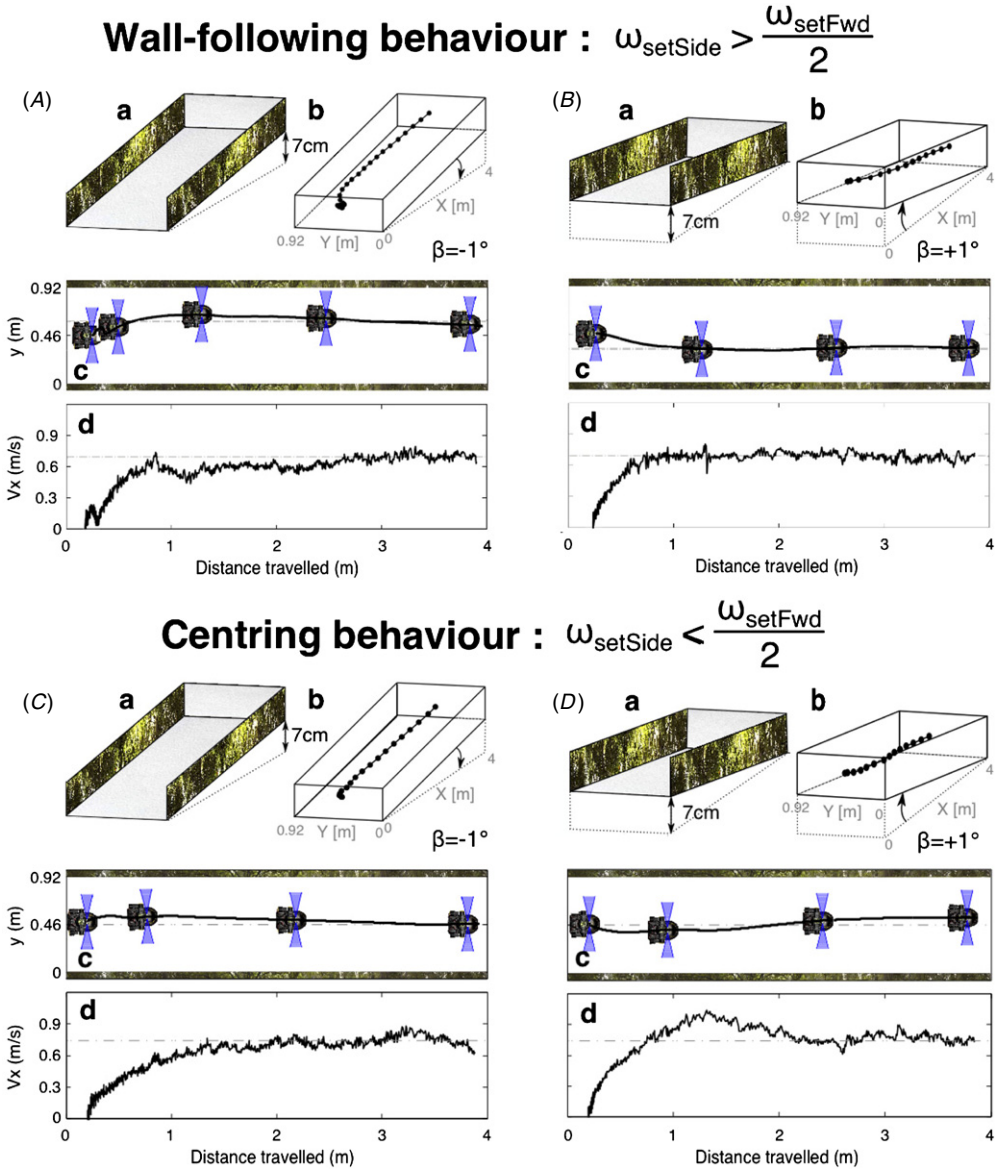

Figure 8. Compensation for an ascending terrain (*A*) and (*C*) or a descending terrain (*B*) and (*D*) by the robot navigating along a straight 4 m long corridor adopting a wall-following behaviour (*A*) and (*B*) or a centring behaviour (*C*) and (*D*). The LORA robot was regulating optic flow using $\omega_{\text{setFwd}} = 190^\circ\ \text{s}^{-1}$ and $\omega_{\text{setSide}} = 125^\circ\ \text{s}^{-1}$ OF set-points for the wall following behaviours and $\omega_{\text{setFwd}} = 190^\circ\ \text{s}^{-1}$ and $\omega_{\text{setSide}} = 80^\circ\ \text{s}^{-1}$ OF set-points for the centring behaviours. Perspective views of the straight 4 m corridors on an ascending terrain ($\beta = -1^\circ$ (*Aa*)and (*Ca*)) or a descending terrain ($\beta = +1^\circ$ (*Ba*) and (*Da*)). ((*Ab*), (*Bb*), (*Cb*), (*Db*)) 3D trajectories of the robot plotted every 0.4 s. Chronophotograph of the hovercraft robot in the horizontal plane. Marks on the trajectories indicate the robot's position and orientation at 2.2 s time intervals (*Ac*) and (*Cc*) and 1.7 s time intervals (*Bc*) and (*Dc*). ((*Ad*), (*Bd*), (*Cd*), (*Dd*)) Forward speed profiles of the trajectories respectively shown in ((*Ac*), (*Bc*), (*Cc*), (*Dc*)). Adopting a wall-following behaviour, the LORA robot followed—in the steady state—the nearest wall perfectly at a constant clearance of $D_{R,L\infty} = 0.31$ m and kept its forward speed constant despite the slope of the terrain, reaching a 'cruising' speed of $V_{f\infty} = 0.69\ \text{m s}^{-1}$. Adopting a centring behaviour, the LORA robot centred and kept its forward speed constant despite the slope of the terrain, reaching a 'cruising' speed of $V_{f\infty} = 0.69\ \text{m s}^{-1}$. The robot equipped with the *dual OF regulator* therefore compensated efficiently for the *physical disturbance* due to the ascending and descending terrains.

the robot on a flat terrain (equations (1) and (3), $\beta = 0^\circ$, see table 2), the speed limit $V_{\text{f max}}$ can be expected to be

$$V_{\text{f max}} = \lim_{t \to +\infty} K_{\text{Fwd}} \cdot u_{\text{f max}} \cdot (1 - \exp^{-\frac{t}{\tau_{\text{Fwd}}}}) = 1.81\ \text{m s}^{-1}. \tag{19}$$

The *unilateral OF regulation* of the sideways control systems makes the clearance from the nearest wall followed proportional to the sideways OF set-point ω_{setSide} (Serres *et al* 2008b). We therefore have:

$$D_{L\infty} = \frac{V_{f\infty}}{\omega_{\text{setSide}}} \text{ with } V_{f\infty} \leqslant V_{\text{f max}}. \tag{20}$$

If the corridor had been long enough, the robot could therefore have been expected to reach a steady clearance from the left wall of $D_{L\infty} = 0.83$ cm when reaching a speed limit of $V_{\text{f max}} = 1.81\ \text{m s}^{-1}$ (equation (19)). This result is therefore consistent with those published on honeybees (Kirchner and Srinivasan 1989, Srinivasan *et al* 1991) flying along a straight,

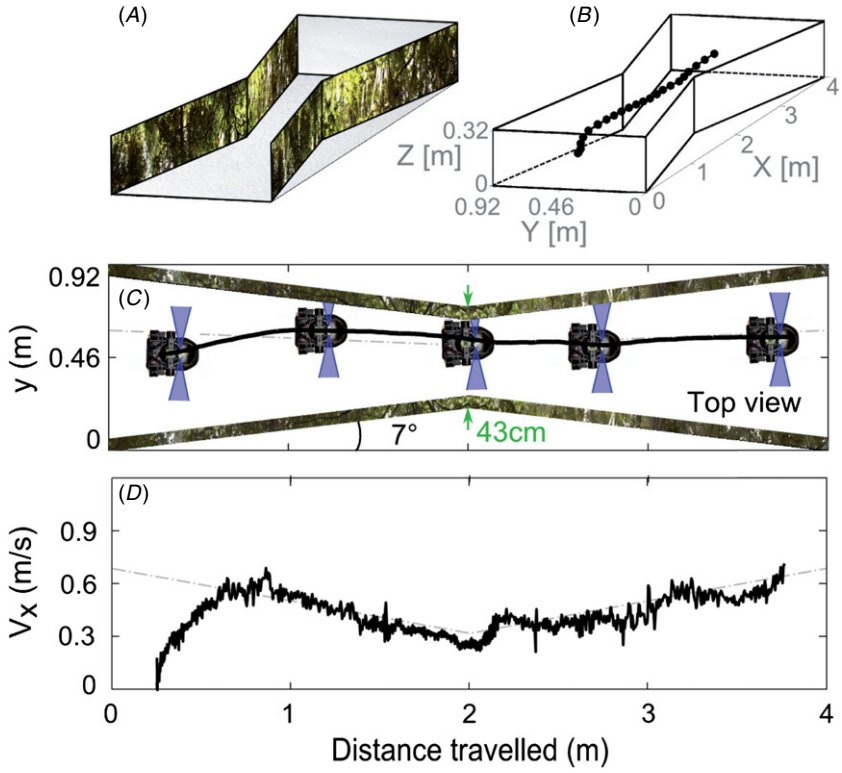

Figure 9. Automatic speed control of the hovercraft robot in a 4 m long tapered corridor (tapering angle: 7°) with a 0.92 m wide entrance and a 0.43 m wide constriction located halfway. When entering the corridor, the robot had no information about the corridor's configuration. (*A*) Perspective view of the 7° tapered corridor. (*B*) 3D trajectory of the hovercraft robot navigating along the tapered corridor, plotted every 0.4 s. (*C*) Chronophotograph of the hovercraft robot in the horizontal plane. Marks on the trajectory indicate the robot's position and orientation at 2.17 s time intervals. In the steady state, the robot showed *wall-following* behaviour, travelling at a safe clearance from the nearest wall. (*D*) Forward speed profiles V_f corresponding to the trajectory shown in (*C*). The forward speed happens to be a linear function of the distance x travelled, and it is therefore proportional to the local corridor width D (grey dash–dotted lines). The robot therefore automatically decelerated when the walls narrowed and speeded up when the walls widened. The narrowing walls are treated by the LORA autopilot like an *OF disturbance*. These results show that the *dual OF regulator* rejected this disturbance efficiently.

Table 2. Identified forward dynamics in function of the lift-fan control signal.

u_{LiftFan} (%)	K_{Fwd} (10^{-3} m s^{-1} · %$^{-1}$)	τ_{Fwd} (s)	Fit factor(%)
42	30.11	2.67	99.8
41	28.11	2.64	99.3
40	25.91	2.63	99.7
39	20.88	2.02	99.4
38	18.45	1.54	98.3
37	16.29	1.34	96.1

Table 3. Identified side dynamics in function of the lift-fan control signal

u_{LiftFan} (%)	K_{Side} (10^{-3}m s^{-1} · %$^{-1}$)	τ_{Side} (s)	Fit factor(%)
42	16.28	2.54	94.32
41	13.92	2.45	92.28
40	11.02	2.2	92.11
39	8.76	1.89	89.12
38	8.32	1.48	88.72
37	7.58	1.2	84.54

narrow corridor, one wall of which was covered with a structureless grey sheet.

In the tapered corridor configurations (figures 11(*E*) and (*F*)), the LORA robot managed to avoid a lateral obstacle successfully by rejecting the strong OF disturbances encountered in both the 7° and 14° tapered corridors, although it adopted the starting position y_0. The robot roughly stabilized its position $D_{L\infty}$ at the end of the course (equation (20)). The marks on the trajectories show that the LORA robot slowed down when approaching the narrowest point and speeded up beyond that point, even in the absence of texture on the right wall. Whatever the corridor configuration (straight or tapered), the robot never rushed into the 'no contrast' zone on the right wall and always followed the textured wall, i.e., the left wall. However, the LORA robot crashed into the left wall after taking the starting position $y_0 = 0.77$ m (figure 11(*F*)), since this position was too close to the wall: the 2 pixel 90° optical direction LMS was not sufficiently informative to make the robot avoid the wall and additional frontal ±45° LMSs were therefore necessary (see figure 10(*E*) and section 5.1).

These results show that our vision-based autopilot enabled the hovercraft to safely avoid a lateral obstacle in both straight and tapered corridors successfully based on the measurements performed by a single 2-pixel LMS, without being greatly disturbed by the absence of contrast on the opposite side.

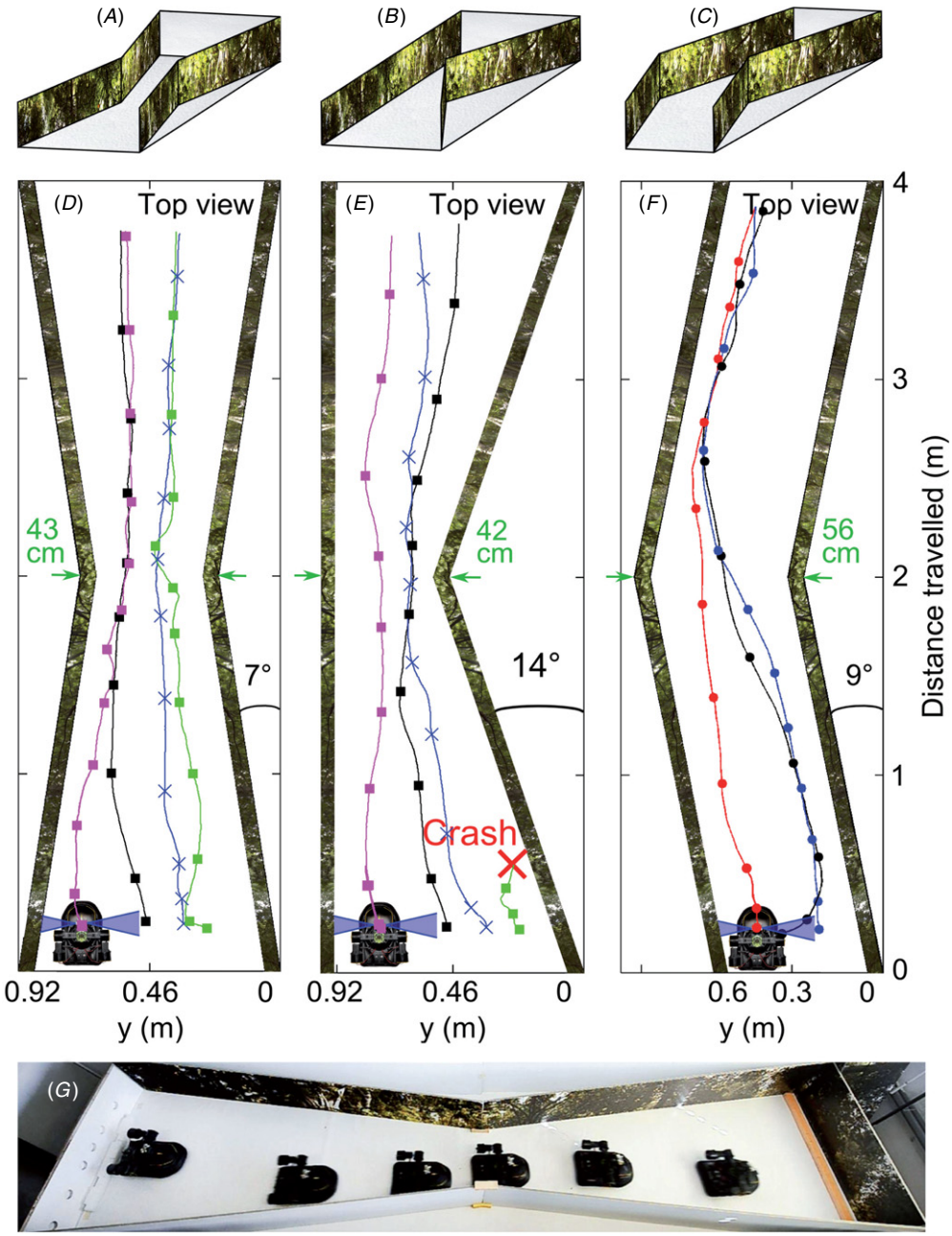

Figure 10. Automatic *wall-following* behaviour as a function of the initial ordinate y_0 in both tapered (7° and 14°) and 18° bend corridors. (*A*) and (*B*) Perspective views of the 4 m long 7° and 14° tapered corridors with a 0.92 m wide entrance and a 0.43 m and 0.42 m wide constriction located midway, respectively. (*C*) Perspective view of the 4 m long 18° bend corridor with a constant local corridor width of 0.56 m. (*D*)–(*F*) Set of trajectories of the LORA robot navigating along the 7° and 14° tapered corridors and the 18° bending corridor in the case of several starting positions y_0. (*G*) Chronophotograph of the robot corresponding to the trajectory shown in (*D*), i.e., the black trajectory, with a 1.67 s time interval. The initial ordinate y_0 was treated by the *dual OF regulator* as a disturbance, and the results of these navigation tests show that the robot performed *wall-following* behaviour despite the unfavourable initial ordinate. The vision-based autopilot therefore rejected this perturbation. However, after adopting the starting position $y_0 = 0.16$ m in the 14° tapered corridor (*E*), the robot crashed into the right wall of the corridor. The 2 pixels detecting the right visual field did not enable the robot to avoid this lateral obstacle.

4.4. Automatic reaction to an 'optic flow step perturbation' introduced by a moving wall

The corridor built for this experiment was a straight, non-stationary 4 m long, 0.92 m wide corridor (figure 12(*A*)). The 4 m left and right walls were lined with a natural panorama depicting trees and bushes. A 1.5 m long part of the left wall (between abscissa $x = 1.75$ m to $x = 3.25$ m) consisting of a rotating band displaying the same panorama was stretched between two vertical drums. A speed-regulated motor made the printed band move forward or backward at a speed of $V_p = \pm 0.30$ m s^{-1} via a V-belt.

Figure 12(*C*) shows superimposed trajectories recorded under three initial band speed conditions with $V_p = \{-0.30; 0; +0.30$ m s$^{-1}\}$. Similar *wall-following* behaviour

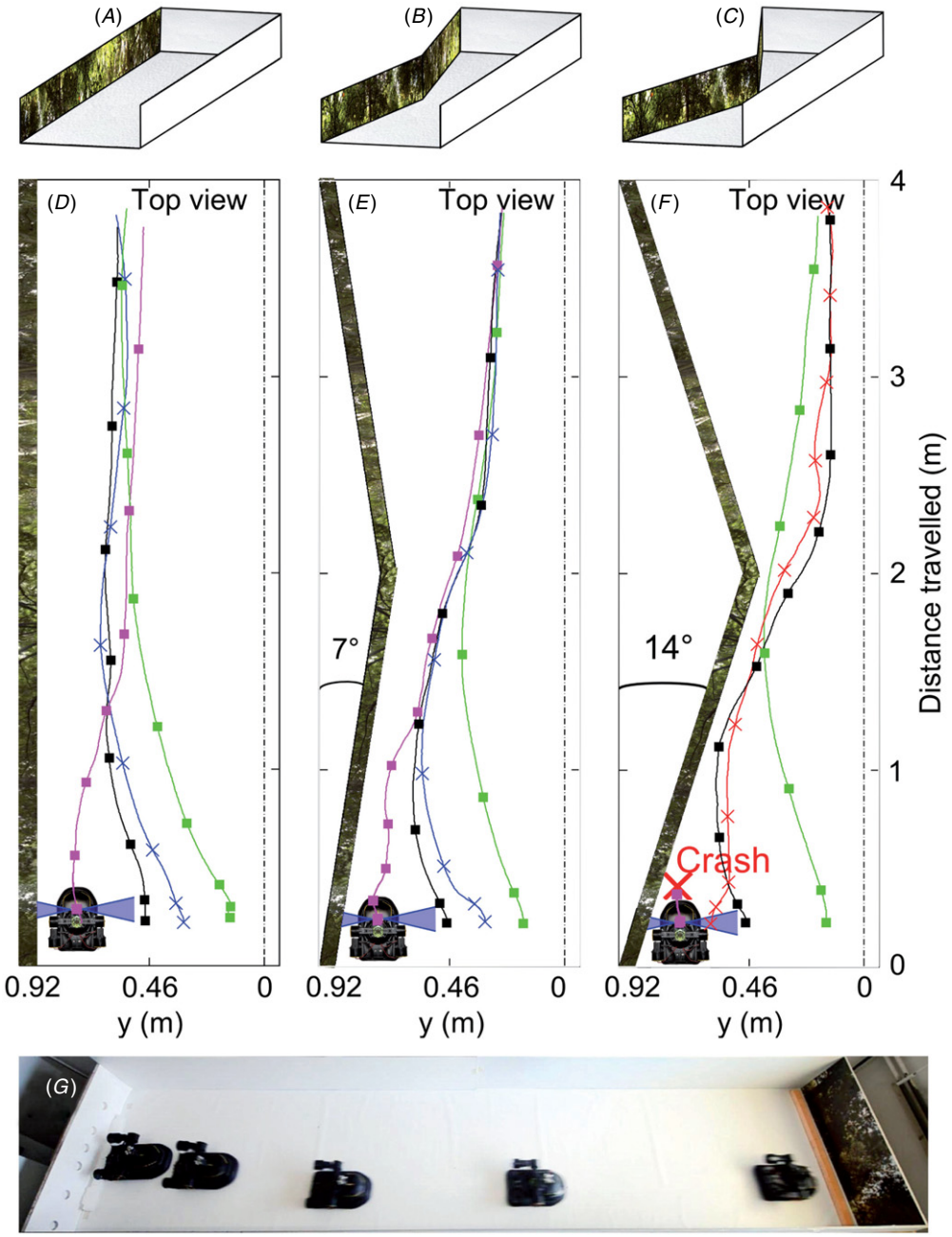

Figure 11. Automatic reaction to a 4 m 'no-contrast' zone in straight and tapered corridors. Since the right wall was devoid of texture (a uniform wall), only the left 2 pixel LMS could feed the autopilot with visual motion measurements/cues. (*A*)–(*C*) Perspective view of the 4 m long straight and tapered corridors (*B*) and (*C*), with tapering angles of 7° and 14°, respectively). (*D*)–(*F*) Set of trajectories of the LORA robot navigating along the straight and tapered corridors after adopting several starting positions y_0. Only the two lateral eyes were used here. (*G*) Chronophotograph of the robot's trajectory shown in (*D*) using the black solid line, with a 1.48 s time step. (*F*) The robot navigated safely along each corridor configuration, except when it was moving too close to the wall. Despite the absence of texture on the right wall, the robot therefore managed to hug the left wall (*wall-following* behaviour) in the straight corridor (*D*) and showed safe lateral obstacle avoidance behaviour in the tapered corridors without rushing into the 'no-contrast' zone (*E*) and (*F*), using a visual system consisting of just a single pair of pixels.

was observed here to that occurring in a straight stationary corridor (figure 7(*C*)). The red trajectory is the LORA robot's trajectory when the left wall was moving at a constant speed ($V_p = +0.30$ m s^{-1}) in the *direction of travel* of the robot. When the robot entered this non-stationary section, it can be seen that it moved closer to the moving wall. The green trajectory (figure 12(*C*)) was recorded in the opposite situation, where the rotating band was moving *against the direction of travel* ($V_p = -0.30$ m s^{-1}). The robot can be seen here to have shifted away from the moving wall. To understand how these shifts towards or away from the moving wall occurred, it is necessary to imagine that the stripe speed V_p on the left wall was perceived by the vision-based autopilot like an 'OF step perturbation' of $-\frac{V_p}{y}$ affecting both the forward

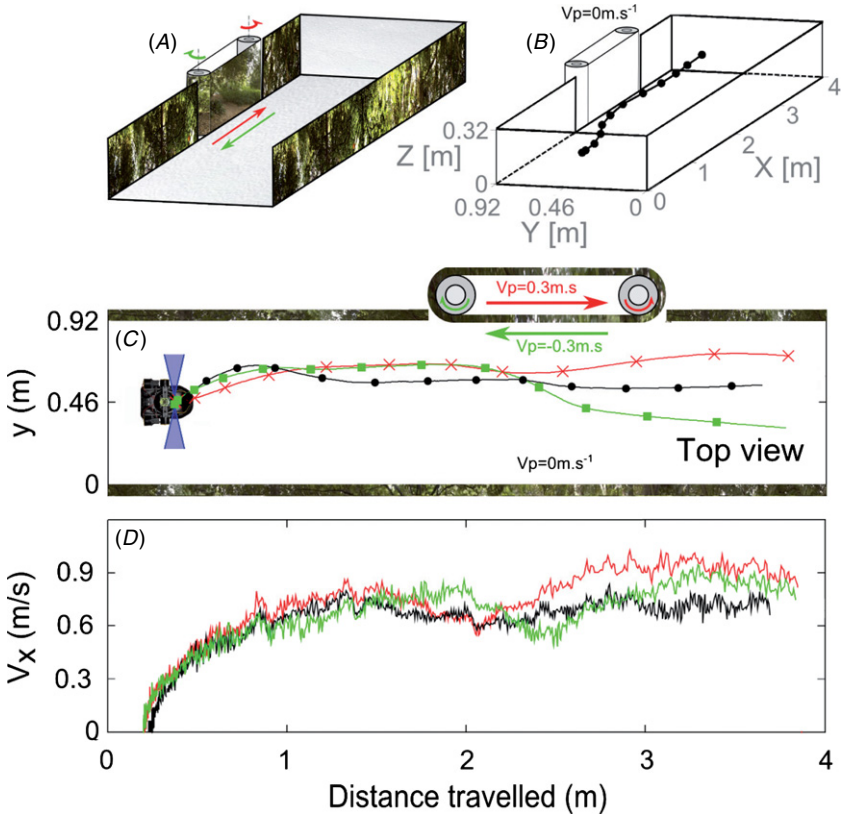

Figure 12. Automatic reaction to the 'OF step perturbation' resulting from a non-stationary section of the left wall from abscissa $x = 1.75$ m to $x = 3.25$ m. The wall was set in motion via a band stretched between two actuated drums. The walls and the strip band were lined with a natural coloured panorama. A set of three experiments was performed, corresponding to three initial band speed conditions $V_p = \{-0.3; 0; 0.3\ \text{m s}^{-1}\}$. (*A*) Perspective view of the non-stationary corridor and the two drums. (*B*) 3D trajectory of the LORA robot plotted every 0.4 s. The band was not set in motion here ($V_p = 0\ \text{m s}^{-1}$). (*C*) Trajectories of the LORA robot under the three initial band speed conditions [$V_p = \{-0.3; 0; 0.3\ \text{m s}^{-1}\}$] (green, black and red trajectories, respectively). The robot started on a central course and then followed the *nearest* wall, i.e., the left wall, and when entering the non-stationary section of the corridor, it either approached the left wall or moved away from it, depending on the direction in which the belt was moving. In the case of the black trajectory ($V_p = 0\ \text{m s}^{-1}$), the robot navigated at a constant clearance from the wall ($D_{L\infty} = 0.31$ m). This behaviour of the robot in a non-stationary corridor is consistent with findings made by Kirchner and Srinivasan (1989) and Portelli *et al* (2010) on honeybees flying along a non-stationary corridor. (*D*) Speed profiles of the robot's trajectories. The forward control system responsible for keeping the sum of the two lateral OFs ($\Sigma\omega_{R,L}^{\text{fused}}$) constant rejected the 'OF step perturbation' due to the moving wall by increasing its forward speed (solid red line) or by decreasing its speed (solid green line).

and sideways control loops (figures 4(*B*) and (*C*)). When the speed of the stripe was negative $V_p = -0.3\ \text{m s}^{-1}$, a positive perturbation of $55^\circ\ \text{s}^{-1}$ was applied to the autopilot, whereas $V_p = +0.3\ \text{m s}^{-1}$ generated a negative OF step perturbation of $-55^\circ\ \text{s}^{-1}$. A negative OF step perturbation in the motion of the wall was taken to mean that the moving wall was farther away, causing the hovercraft to accelerate while coming closer to the wall (figures 12(*C*) and (*D*), red solid line); and conversely, when a larger OF was measured, the opposite effect occurred (the green solid line in figures 12(*C*) and (*D*)).

These results obtained with the *dual OF regulator* therefore account for the previous findings made on bees in a non-stationary corridor (Kirchner and Srinivasan 1989, Srinivasan *et al* 1991, Baird *et al* 2005).

4.5. Automatic navigation in a 18° bending corridor

The experiments described in this section were performed with a bending 4 m long, 0.56 m wide corridor with an 18° bend located halfway. A perspective view of this corridor lined with natural panoramas is shown in figure 10(*C*). This corridor was built to test the navigation performances of the LORA robot when it was no longer aligned with the local longitudinal axis of the corridor.

In this 18° bending corridor, the robot was made to adopt several initial starting positions with $x_0 = 0.25$ m and $y_0 = \{0.16; 0.2; 0.44\ \text{m}\}$ (figure 10(*F*)). The heading-lock feedback loop was constantly set so as to align the robot's body with the 0° orientation, which is the mean corridor orientation. The corridor walls formed an angle of +9° with the longitudinal axis of the corridor in the first half and an angle of −9° in the second half of the corridor. The results presented in figure 10(*F*) show that the robot navigated safely along the corridor regardless of its starting position y_0 and that it showed *wall-following behaviour despite the non-alignment of the robot's body axis with the local longitudinal axis of the corridor*. The robot also switched between following the right and left walls (black and blue trajectories, figure 10(*F*)) because the *sign* function (figure 4(*C*)) selected the direction corresponding to the nearest wall ($\min(D_{L,R})$). In the second

part of the bending corridor, the robot hugged the left wall rather too closely because of the lack of visual motion sensors in its frontal part. As the corridor width was constant ($D = 0.56$ m), the forward speed was kept roughly constant at $V_f = 0.42$ m s^{-1}.

5. Experimental results obtained with a 8 pixel compound eye

In this section, our previous compound eye was improved by adding two LMSs, i.e., two pairs of pixels in the frontal part facing at an azimuthal angle of $\pm 45^\circ$ in order to obtain a minimalistic compound eye consisting of four pairs of pixels connected to four LMSs. The two extra frontal eyes were intended to help the robot navigate in more demanding to 'extreme' corridor configurations. The forward 45° eye detects the lateral OF before the lateral eye. When looking forward, the robot is therefore endowed with a kind of prediction horizon that helps it to reject lateral disturbances. This prediction horizon (in seconds) can be computed as follows:

$$\tau_0 = \frac{1}{\omega_R} = 0.46 \text{ s}. \tag{21}$$

Therefore, after being endowed with this prediction horizon, the robot can negotiate the 14° tapered corridor more easily and avoid colliding with the wall.

Visual motion signals were fused as in equations (15) and (16) to generate the left and right visual motion signals (ω_L^{fused} and ω_R^{fused}, respectively). The OF set-points were set at $\omega_{\text{setFwd}} = 190^\circ$ s^{-1} and $\omega_{\text{setSide}} = 125^\circ$ s^{-1}.

5.1. Safe navigation in stringent corridor configurations with two additional frontal eyes

The LORA robot was therefore tested in a 7° tapered corridor (figure 13(*A*)), a 14° unilateral tapered corridor (figure 13(*B*)) and a 18° bending corridor (figure 13(*C*)) to assess the navigation performances of the latest version of the LORA robot equipped with this novel compound eye.

The trajectories of the LORA robot with several starting positions y_0 in the tapered and bend corridors are presented in figures 13(*D*)–(*F*). The robot showed perfect *wall-following* behaviour in each of the corridor configurations tested, regardless of its starting position y_0. Marks on the trajectories show that the robot also controlled its speed depending on the local corridor width. It is worth mentioning that in the case of the initial ordinate $y_0 = 0.16$ m in the 14° tapered corridor, the robot avoided the right wall and followed it at a safe clearance, whereas it crashed into the wall when it was equipped only with its original 4 pixel compound eye (figures 10(*F*) and 14(*F*)). In the 18° bend corridor, the robot kept a wider clearance from the nearest wall (figure 13(*F*)) than it did with a purely $\pm 90^\circ$ lateral vision system (figure 10(*F*)), which confirms that frontal eyes improved the ability of the LORA robot to navigate safely in challenging corridor configurations by preventing lateral collisions.

5.2. Repeatability of the LORA robot's performances with an 8 pixel compound eye

Figure 14(*G*) shows 12 successive trials in a 14° tapered corridor. The grey dash–dotted lines give the steady-state clearance of the LORA robot from the nearest wall with the OF set-points $\omega_{\text{setFwd}} = 190^\circ$ s^{-1} and $\omega_{\text{setSide}} = 125^\circ$ s^{-1}. Unlike the trajectory of the robot equipped with a 4-pixel visual system (figure 14(*F*)), the mean trajectory recorded here (figure 14(*G*), red solid line) shows that the robot navigated successfully along the 14° tapered corridor without crashing into the wall during 12 successive trials (figure 14(*G*)). The robot therefore showed more reliable *wall-following* behaviour, thanks to the addition of the $\pm 45^\circ$ optical directional eyes, which improves the two visual feedback signals controlling the dual OF regulator equipping the LORA robot.

6. Repeatability of the LORA robot's performance with a 4 pixel and 8 pixel compound eye

Figure 14 gives the results of a repeatability study on the LORA robot based on a set of 12 successive trajectories in one straight (figure 14(*A*)) and two tapered corridors (figures 14(*B*) and (*C*)) with tapering angles of 7° and 14°. The mean trajectory (red solid line) and the standard deviation of the mean (pink shaped area) were calculated based on a set of 12 recorded trajectories. The robot was equipped with the 4 pixel visual system shown in figures 14(*D*)–(*F*)) (where the FOVs are given by a blue conical shape).

In both the straight and 7° tapered corridors (figures 14(*D*) and (*E*)), the LORA robot entered the corridor in a central position and achieved safe *wall-following* behaviour by controlling both its speed and its clearance from the walls on the sole basis of OF cues during the 12 successive trajectories. The mean trajectory and the standard deviation of the mean show that the robot achieved excellent performances in terms of the repeatability and reliability of the *dual OF regulator* used to guide the robot equipped with an eye consisting of only 4 pixels along hitherto unknown corridors. However, when the robot started off too near the wall ($y_0 = 0.16$ m, figure 14(*F*)) of the 14° tapered corridor, it crashed in all 12 successive trials, which shows the limitations of using only a 4 pixel compound eye to navigate in highly challenging corridors.

This limitation can be explained theoretically in the case of tapered corridors regardless of the robots dynamics. In the case of the dual OF regulator (based on forward and side control laws) used here, it has been established by Serres *et al* (2008a) that the forward speed varies exponentially with time in tapered corridors. The visual closed-loop time constant can therefore be computed as follows:

$$\tau(\alpha) = \frac{\omega_{\text{setFwd}}}{2 \cdot \tan(\alpha) \cdot \omega_{\text{setSide}} \cdot (\omega_{\text{setFwd}} - \omega_{\text{setSide}})} \tag{22}$$

with $\omega_{\text{setFwd}} = 190^\circ$ s^{-1}, $\omega_{\text{setSide}} = 125^\circ$ s^{-1}.

Equation (22) gives a strong criterion for choosing appropriate OF set-points in terms of the safe navigation. For example, in the case where $\alpha = 7^\circ$, equation (22) shows that the robot has to decelerate and reach its steady forward speed with a maximum time constant of $\tau(7^\circ) = 5.49$ s to avoid

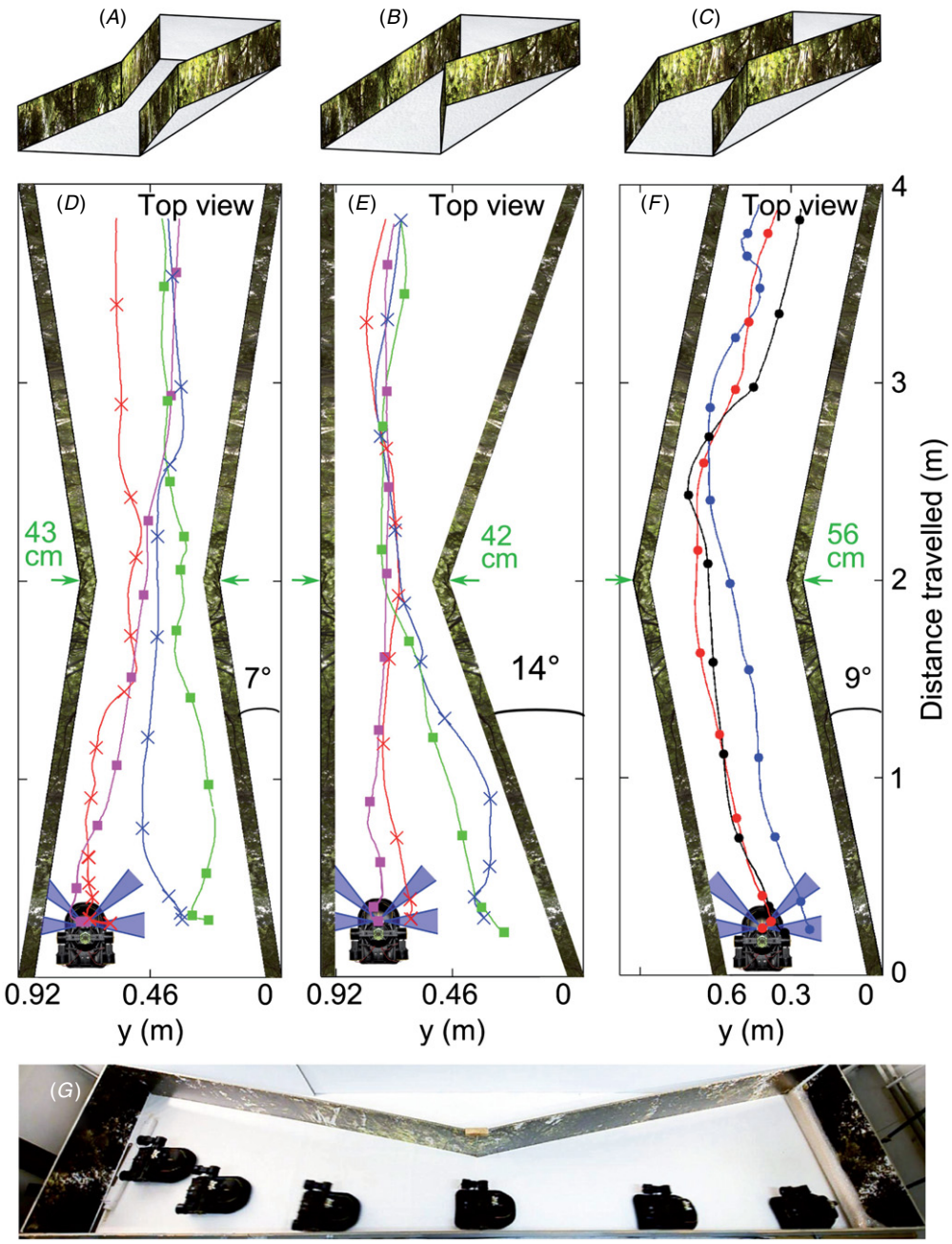

Figure 13. Robust navigation in highly challenging corridor configurations in both tapered (7° and 14°) and 18° bend corridors thanks to the two additional frontal eyes. (*A*)–(*C*) Perspective views of the 4 m long tapered corridors ((*A*) and (*B*)), 7° and 14°) and the 18° bend corridor. (*D*)–(*F*) Set of trajectories of the LORA robot navigating along the tapered corridors ($y_0 = \{0.16; 0.31; 0.46; 0.61; 0.77$ m$\}$) and the 18° bend corridor $y_0 = \{0.16; 0.28; 0.44$ m$\}$. (*G*) Chronophotograph of the robot shown in (*E*) by a solid red line, with a 1.48 s time step. In comparison with the two-eyed robot (figure 10), the LORA robot gave better navigation performance since it never crashed into the walls (*E*) and travelled at a safer clearance from the walls (*F*).

crashing. As the robot is endowed with a forward dynamic time constant of $\tau_{\mathrm{Fwd}} = 2.67$ s, its dynamics are fast enough to cope with the dual OF regulation laws and therefore to decelerate safely. However, in the case where $\alpha = 14°$, equation (22) shows that the robot must decelerate and reach its steady forward speed with a time constant of $\tau(14°) = 2.7$ s, which is very similar to its own dynamics τ_{Fwd}. In this 14° tapered corridor configuration, the robot therefore cannot decelerate fast enough to reach its safe steady forward speed in time and it therefore crashes into the wall.

7. Discussion

Here we present a complete benchmark for a miniature *fully actuated* hovercraft (figure 1(*A*)) equipped with a bee-inspired autopilot named LORA. The performances of the robot endowed with a minimalistic visual system (consisting of only four or eight pixels forming up to four local motion sensors (LMSs) show that the hovercraft can navigate safely under purely visual control along challenging unknown corridors such as bending corridors and a straight corridor over flat or

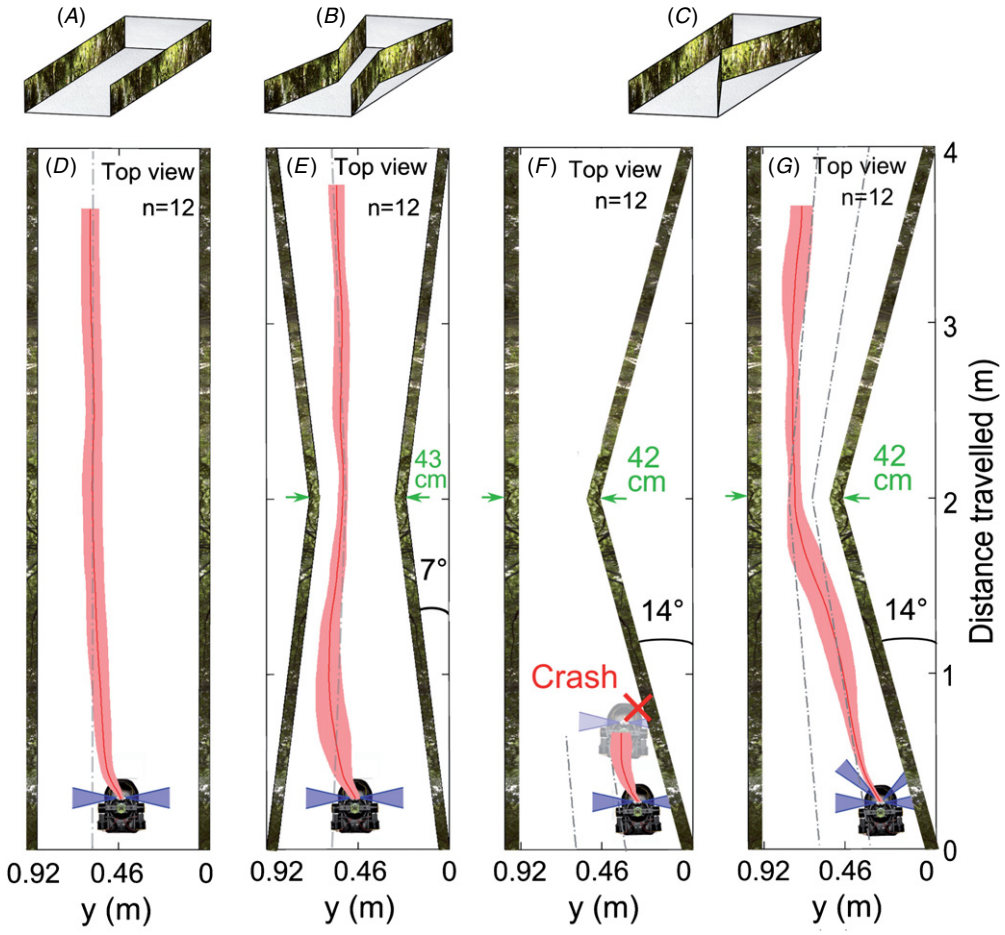

Figure 14. Study on the repeatability of the performance of the two-eyed LORA robot (*D*)–(*F*) and those of the four-eyed robot (*G*). (*A*)–(*C*) Perspective views of the 4 m long straight and tapered corridors. (*D*)–(*F*) Repeatability of the LORA robot's trajectory equipped with two ±90° lateral eyes. The mean trajectory (solid red line) and the standard deviation of the mean (pink shaded area) were computed from a set of 12 trajectories and plotted with the expected/predicted steady-state position (grey dash–dotted line). The robot showed efficient *wall-following* behaviour in both straight and 7° tapered corridors. The mean trajectory (solid red line) matched the expected/predicted steady-state position very closely. As depicted in 13(*E*), the visual system did not prevent the robot from crashing into the wall. (*G*) The four-eyed robot showed efficient *wall-following* behaviour and alternately avoided both the right and left walls. All the trajectories shown here resulted from the *dual OF regulators* scheme with $\omega_{\text{setFwd}} = 190^\circ\ \text{s}^{-1}$ and $\omega_{\text{setSide}} = 125^\circ\ \text{s}^{-1}$.

sloping terrain (figures 6(*A*), 6(*C*), 7 and 8), even when one wall is devoid of texture (figure 11), or when one wall is moving (figure 12), and even when the corridor narrows or bends on the horizontal plane (figures 6(*B*), 6(*D*), 9, 10 and 13). The 8 pixel compound eye was implemented on the LORA robot to improve its lateral obstacle avoidance performances in demanding corridor configurations (figure 13) by increasing the optical directions to ±45°. The LORA's robustness to strong physical OF disturbances was also tested. The lack of contrast on one side (figure 11), tapered corridors (figures 9, 10 and 13) and a moving wall (figure 12) were treated by the LORA autopilot like strong OF perturbations and a positive or negative sloping terrain was handled in the same way as an external physical disturbance such as a headwind or tailwind.

Fully actuated robots can be endowed with these navigation skills by equipping them with a minimalistic visual system consisting of only 4 or 8 pixels, i.e., two or four 2 pixel LMSs, forming a primitive insect-inspired visual system requiring few computational resources. The LORA autopilot guides the hovercraft in the 2D horizontal plane, avoiding the walls by performing manoeuvres involving only translational degrees of freedom along the *x*- and *y*-axis. The keystone of the LORA autopilot is the *heading-lock* system, which enables the robot to experience a purely translational OF and the pair of intertwined OF regulators forming the *dual OF regulator* which strives to hold the perceived OF constant by adjusting both the forward and side thrusts. Bees are likewise equipped with a heading-lock system based on polarized light cues (von Frisch 1948), which enables these insects to take an impressively straight course even in the presence of wind (Riley and Osborne 2001).

Figure 15 shows the similarities existing between the performances of bees observed during the last 25 years in ethological studies and those of our robot equipped with the *dual OF regulator*, tested in similar situations. As summarized in the latter figure, the explicit LORA control system (figure 4) may provide a possible explanation for the behaviour of free-flying bees along a stationary (Kirchner and Srinivasan 1989, Srinivasan *et al* 1991, Baird *et al* 2005, Serres *et al*

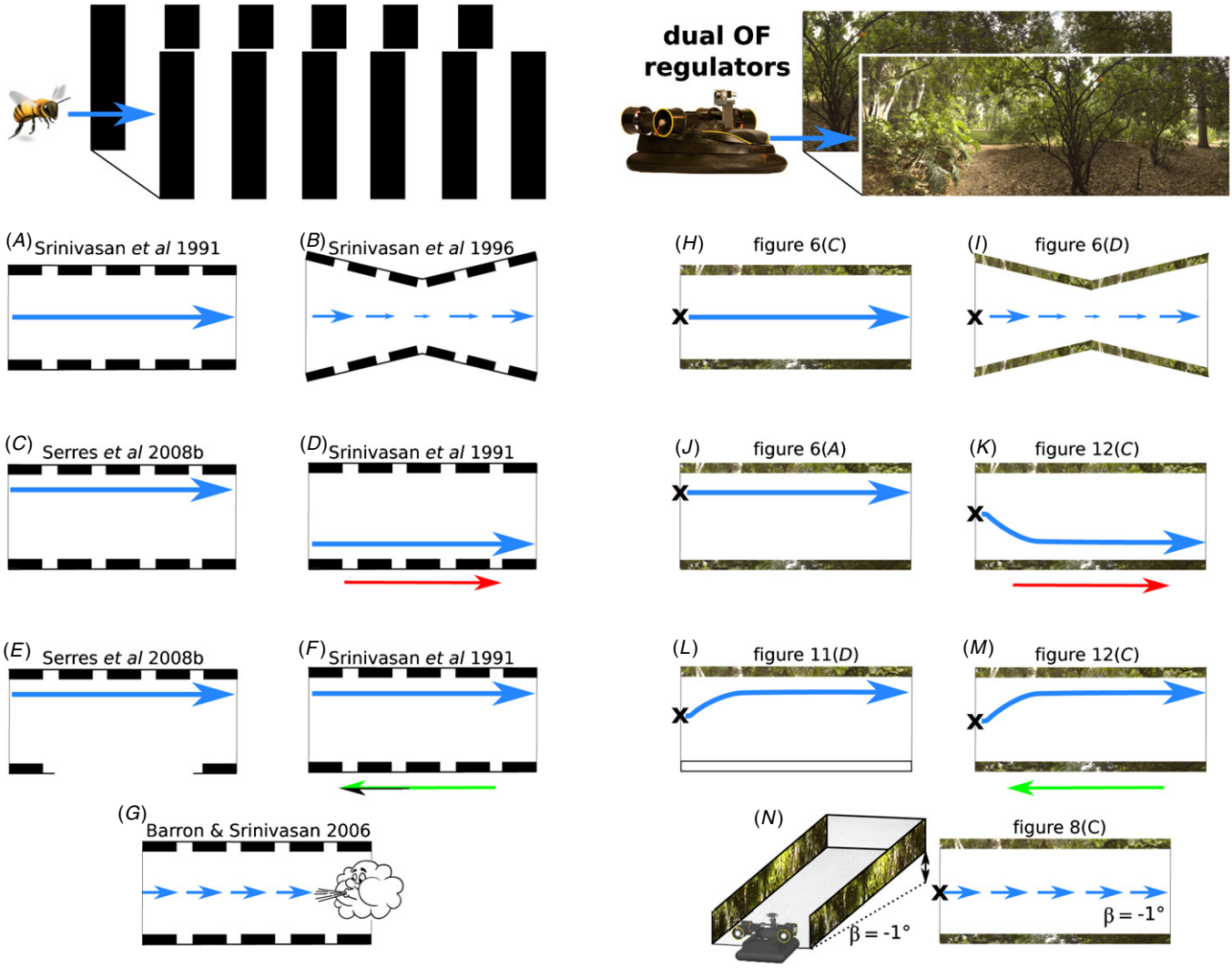

Figure 15. Summary of the similarities of the bee behaviours observed in the last 25 years ethological studies (*A*)–(*G*) and the *fully actuated* robot behaviours equipped with the bee-inspired LORA autopilot tested in similar situations (*H*)–(*N*). These results show the *dual OF regulator* combined with heading-lock system can be viewed as a working hypothesis to explain how the honeybee *Apis Melliphera* controls both its speed and position on the horizontal plane of a constraint corridor. Blue arrows represent the main direction of the agent moving in a corridor where the entrance is represented by a cross. Red and green arrows represent the direction of motion of the moving wall in case of a non-stationary corridor. The last comparison (*G*) versus (*N*) shows how constant speed behaviour despite head wind may be explained by the presented model.

2008b) or non-stationary corridor (Kirchner and Srinivasan 1989, Srinivasan *et al* 1991, Portelli *et al* 2010) or a tapered corridor (Srinivasan *et al* 1996, Portelli *et al* 2011) or even a corridor in which no texture is present on one wall (Kirchner and Srinivasan 1989, Srinivasan *et al* 1991), mimicking the effect of an 'aperture' (Serres *et al* 2008b) or again in the presence of wind (Barron and Srinivasan 2006). This autopilot was designed in line with the Gibsonian viewpoint (Gibson 1950) according to which an animal's visual system drives the locomotor system without any representation of the environment (Pichon *et al* 1989, Franceschini *et al* 1992, Duchon and Warren 1994).

The *direction control system* based on the *sign* function (figure 4(*C*)) may restrict the robot's manoeuvres, as it acts only as a 'reflex' mechanism, making the robot always head towards the nearest wall ($\min(D_{L,R})$, and hence $\max(\omega_{L,R})$ in figure 4(*C*)).

The sideways control system with which the LORA autopilot is equipped makes the robot's trajectory highly dependent on the corridor's configuration (as can be seen in figure 10(*E*) and 10(*F*)). The robot is therefore always bound to aimlessly follow the nearest wall. For instance, an artificial bee equipped with the LORA autopilot (with OF set-points typical of *wall-following* behaviour) entering the left entrance of a straight corridor would never reach a reward placed near the right wall at the end of the corridor, because the artificial bee would always follow the left wall as long as no other set of OF set-points is provided to make it switch from one wall to the other.

8. Conclusion

In conclusion, our autonomous hovercraft was able to travel at high optic flows ($125^\circ\ s^{-1}$) along challenging

unfamiliar corridors such as non-stationary corridors and those comprising 'no contrast' zones, tapered and bent corridors and even a sloping terrain, using very few pixels (4 or 8 pixels) without any need for *metric sensors such as rangefinders or velocimeters*. We have also reported above how we have improved the navigation performances of the robot under exacting corridor conditions by adding two frontal eyes. The LORA autopilot based on the *dual OF regulator* combined with a heading-lock system is the first step to designing a deft, lightweight (the autopilots electronics weigh only 8.17 g), power-lean (power consumption: 0.75 W) low-cost visuomotor control system which could be potentially installed on a 3D free-flying micro-air vehicle by adding a ventral and a dorsal *OF regulator* making it capable of performing ground following, ceiling following or even docking tasks such as those tested in Expert and Ruffier (2012). This autopilot also suggests new ways of finding solutions to the automatic guidance of other types of holonomic and fully actuated vehicles such as blimps, underwater vehicles, quadrotors and even helicopters with counter-rotating rotors (in which the pitch and roll axes are uncoupled).

The next step will consist in exploring other visual fusion strategies, especially that based on an anticipatory feedforward system involving the $\pm 45^{\circ}$ lateral eyes, such as those tested in Ruffier and Franceschini (2008) to help the robot anticipate and achieve lateral obstacle avoidance. We also intend to enlarge the robots field of view in the central part of the visual field, for example with the panoramic CurvACE sensor (Floreano *et al* 2013), to improve the OF measurements and enable the robot to negotiate even more challenging corridors comprising L-junctions or T-junctions successfully.

Acknowledgments

We are grateful to the reviewers who helped us to improve the paper and clarify our statements. We thank R Brinkworth and D O'Carroll (Adelaide University, Australia) for kindly making their high dynamic range panoramic images available to us, J Diperi and Y Luparini for their involvement in the mechanical design of the LORA robot and the test bench, M Boyron for his involvement in the overall electronic design of the LORA robot, A Manecy and T Raharijaona for their fruitful comments and J Blanc for correcting the English paper. This research was supported partly by CNRS (Life Science; Information Science; Engineering Science and Technology), Aix-Marseille University and the French National Research Agency (ANR) (EVA project and IRIS project under ANR grants' number ANR608-CORD-007-04 and ANR-12-INSE-0009, respectively).

References

Argyros A, Tsakiris D and Groyer C 2004 Biomimetic centering behavior mobile robots with panoramic sensors *IEEE Robot. Autom. Mag.* **11** 21–30

Baird E, Boeddeker N, Ibbotson M R and Srinivasan M V 2013 A universal strategy for visually guided landing *Proc. Natl Acad. Sci.* **110** 18686–91

Baird E and Dacke M 2012 Visual flight control in naturalistic and artificial environments *J. Comp. Physiol.* A **198** 869–76

Baird E, Kornfeldt T and Dacke M 2010 Minimum viewing angle for visually guided ground speed control in bumblebees *J. Exp. Biol.* **213** 1625–32

Baird E, Srinivasan M V, Zhang S and Cowling A 2005 Visual control of flight speed in honeybees *J. Exp. Biol.* **208** 3895–905

Baird E, Srinivasan M, Zhang S, Lamont R and Cowling A 2006 Visual control of flight speed and height in the honeybee *From Animals to Animats 9* vol 4095 ed S Nolfi, G Baldassarre, R Calabretta, J Hallam, D Marocco, J A Meyer, O Miglino and D Parisi (Berlin: Springer) pp 40–51

Baratoff G, Toepfer C and Neumann H 2000 Combined space-variant maps for optical flow navigation *Biol. Cybern.* **83** 199–209

Barron A and Srinivasan M V 2006 Visual regulation of ground speed and headwind compensation in freely flying honey bees (Apis mellifera L.) *J. Exp. Biol.* **209** 978–84

Blanes C 1986 Appareil visuel élémentaire pour la navigation à vue d'un robot mobile autonome *Master Thesis* in Neurosciences (DEA in French) Neurosciences (Aix-Marseille II)

Blanes C 1991 Guidage visuel d'un robot mobile autonome d'inspiration bionique *U-Thesis INP Grenoble*

Conroy J, Gremillion G, Ranganathan B and Humbert J S 2009 Implementation of wide-field integration of optic flow for autonomous quadrotor navigation *Auton. Robots* **27** 189–98

Duchon A and Warren W 1994 Robot navigation from a Gibsonian viewpoint *IEEE Int. Conf. on Systems, Man, and Cybernetics. Humans, Information and Technology (San Antonio, USA)* vol 3 pp 2272–7

Dyhr J P and Higgins C M 2010 The spatial frequency tuning of optic-flow-dependent behaviors in the bumblebee Bombus impatiens *J. Exp. Biol.* **213** 1643–50

Eichner H, Joesch M, Schnell B, Reiff D F and Borst A 2011 Internal structure of the fly elementary motion detector *Neuron* **70** 1155–64

Expert F and Ruffier F 2012 Controlling docking, altitude and speed in a circular high-roofed tunnel thanks to the optic flow *IROS'12: Int. Conf. on Intelligent Robots and Systems (Vilamoura, Portugal)* pp 1125–32

Expert F, Viollet S and Ruffier F 2011 Outdoor field performances of insect-based visual motion sensors *J. Field Robot.* **28** 521–41

Floreano D *et al* 2013 Miniature curved artificial compound eyes *Proc. Natl Acad. Sci. USA* **110** 9267–72

Franceschini N, Pichon J M and Blanes C 1992 From insect vision to robot vision *Phil. Trans. R. Soc.* B **337** 283–94

Franceschini N, Riehle A and Le Nestour A 1989 Directionally selective motion detection by insect neurons facets of vision *Facets of Vision* ed D G Stavanga and R C Hardie (Berlin: Springer) pp 360–90

Franceschini N, Ruffier F and Serres J 2007 A bio-inspired flying robot sheds light on insect piloting abilities *Curr. Biol.* **17** 329–35

Franceschini N, Ruffier F, Serres J and Viollet S 2009 Optic flow based visual guidance: from flying insects to miniature aerial vehicles *Aerial Vehicles* (Vienna: In-Tech) pp 747–70

Fuller S and Murray R M 2011 A hovercraft robot that uses insect-inspired visual autocorrelation for motion control in a corridor *ROBIO'11: IEEE Int. Conf. on Robotics and Biomimetics (Karon Beach, Phuket)* pp 1474–81

Gibson J 1950 *The Perception of the Visual World* (Oxford: Houghton Mifflin) p 242

Götz K 1964 Optomotorische untersuchung des visuellen systems einiger augenmutanten der fruchtfliege drosophila *Biol. Cybern.* **2** 77–92

Horridge G 1987 The evolution of visual processing and the construction of seeing systems *Proc. R. Soc.* B **230** 279–92

Humbert J and Hyslop A M 2010 Bioinspired visuomotor convergence *IEEE Trans. Robot.* **26** 121–30
Ibbotson M 2001 Evidence for velocity-tuned motion-sensitive descending neurons in the honeybee *Proc. R. Soc.* B **268** 2195–201
Ijspeert A J, Crespi A, Ryczko D and Cabelguen J-M 2007 From swimming to walking with a salamander robot driven by a spinal cord model *Science* **315** 1416–20
Jin Z, Waydo S, Wildanger E, Lammers M, Scholze H, Foley P, Held D and Murray R 2004 MVWT-II: the second generation Caltech Multi-Vehicle Wireless Testbed *Proc. 2004 American Control Conf. (Boston, USA)* vol 6 pp 5321–6
Kirchner W and Srinivasan M V 1989 Freely flying honeybees use image motion to estimate object distance *Naturwissenchaften* **76** 281–2
Koenderink J and van Doorn A 1987 Facts on optic flow *Biol. Cybern.* **56** 247–54
Pichon J, Blanes C and Franceschini N 1989 Visual guidance of a mobile robot equipped with a network of self-motion sensors *Proc. SPIE* **1195** 44–53
Portelli G, Roubieu F L, Ruffier F and Franceschini N 2011 Honeybees' speed depends on dorsal as well as lateral, ventral and frontal optic flows *PLoS ONE* **6** e19486
Portelli G, Ruffier F and Franceschini N 2010 Honeybees change their height to restore their optic flow *J. Comp. Physiol.* A **196** 307–13
Riley J R and Osborne J L 2001 Flight trajectories of foraging insects: observations using harmonic radar *Insect Movement: Mechanisms and Consequences* ed D R Reynolds and C D Thomas (Wallingford: CABI) chapter 7 pp 129–57
Roubieu F, Expert F, Sabiron G and Ruffier F 2013 Two-directional 1-g disual motion sensor inspired by the fly's eye *IEEE Sensors J.* **13** 1025–35
Roubieu F L, Serres J, Franceschini N, Ruffier F and Viollet S 2012 A fully-autonomous hovercraft inspired by bees; wall-following and speed control in straight and tapered corridors *ROBIO'12: IEEE Int. Conf. on Robotics and Biomimetics (Guangzhou, China)* pp 1311–8
Ruffier F and Expert F 2012 Visual motion sensing onboard a 50-g helicopter flying freely under complex VICON-lighting conditions *CME'12: IEEE Int. Conf. on Complex Medical Engineering (Kobe, Japan)* pp 634–9
Ruffier F and Franceschini N 2005 Optic flow regulation: the key to aircraft automatic guidance *Robot. Auton. Syst.* **50** 177–94
Ruffier F and Franceschini N 2008 Aerial robot piloted in steep relief by optic flow sensors *IROS'08: Int. Conf. on Intelligent Robots and Systems (Nice, France)* pp 1266–73
Santos-Victor J, Sandini G, Curotto F and Garibaldi S 1995 Divergent stereo in autonomous navigation: from bees to robots *Int. J. Comput. Vision* **14** 159–77
Seguchi H and Ohtsuka T 2003 Nonlinear receding horizon control of an underactuated hovercraft *Int. J. Robust Nonlinear Control* **13** 381–98
Seidl R A 1982 Die sehfelder und ommatidien divergenzwinkel von Arbeiterin, Königin und drohn der honigbiene (Apis mellifica) *PhD Thesis* Technische Hochschule Darmstadt
Serres J, Dray D, Ruffier F and Franceschini N 2008a A vision-based autopilot for a miniature air vehicle: joint speed control and lateral obstacle avoidance *Auton. Robots* **25** 103–22
Serres J, Masson G, Ruffier F and Franceschini N 2008b A bee in the corridor: centering and wall-following *Naturwissenschaften* **95** 1181–7
Srinivasan M, Lehrer M, Kirchner W and Zhang S 1991 Range perception through apparent image speed in freely flying honeybees *Vis. Neurosci.* **6** 519–35
Srinivasan M, Zhang S, Lehrer M and Collett T 1996 Honeybee navigation en route to the goal: visual flight control and odometry *J. Exp. Biol.* **199** 237–44
Straw A D, Serin L and Dickinson M H 2010 Visual control of altitude in flying drosophila *Curr. Biol.* **20** 1550–6
Tammero L F and Dickinson M H 2002 The influence of visual landscape on the free flight behavior of the fruit fly *Drosophila Melanogaster J. Exp. Biol.* **205** 327–43
Viollet S, Kerhuel L and Franceschini N 2008 A 1-gram dual sensorless speed governor for micro-air vehicles *16th Mediterranean Conf. on Control and Automation (Ajaccio, France)* pp 1270–75
von Frisch K 1948 Gelöste und ungelöste Rätsel der Bienensprache *Naturwissenschaften* **35** 12–23
Wagner H 1982 Flow-field variables trigger landing in flies *Nature* **297** 147–8
Webb B 2001 Can robots make good models of biological behaviour? *Behavioural Brain Sci.* **24** 1033–50
Weber K, Venkatesh S and Srinivasan M 1997 *Insect Inspired Behaviours for the Autonomous Control of Mobile Robots in From Living Eyes to Seeing Machines* ed M Srinivasan and S Venkatesh (Oxford: Oxford University Press) pp 226–48
Whiteside T and Samuel G 1970 Blur zone *Nature* **225** 94–5
Zufferey J-C and Floreano D 2006 Fly-inspired visual steering of an ultralight indoor aircraft *IEEE Trans. Robot.* **22** 137–46
Zufferey J-C, Klaptocz A, Beyeler A, Nicoud J-D and Floreano D 2007 A 10-gram vision-based flying robot *Adv. Robot.* **21** 1671–84